

Cell autonomous requirement of neurofibromin (Nf1) for postnatal muscle hypertrophic growth and metabolic homeostasis

Xiaoyan Wei^{1,2}, Julia Franke^{1,2}, Mario Ost^{3,4} , Kristina Wardelmann^{5,6}, Stefan Börno⁷, Bernd Timmermann⁷, David Meierhofer⁸ , Andre Kleinridders^{5,6,9} , Susanne Klaus^{3,10}  & Sigmar Stricker^{1,2*} 

¹Musculoskeletal Development and Regeneration Group, Institute of Chemistry and Biochemistry, Freie Universität Berlin, Berlin, Germany, ²Development and Disease Group, Max Planck Institute for Molecular Genetics, Berlin, Germany, ³Department of Physiology of Energy Metabolism, German Institute for Human Nutrition, Nuthetal, Germany, ⁴Department of Neuropathology, University Hospital Leipzig, Leipzig, Germany, ⁵Junior Research Group Central Regulation of Metabolism, German Institute for Human Nutrition, Nuthetal, Germany, ⁶Institute of Nutritional Science, Department of Molecular and Experimental Nutritional Medicine, University of Potsdam, Potsdam, Germany, ⁷Sequencing Core Unit, Max Planck Institute for Molecular Genetics, Berlin, Germany, ⁸Mass Spectrometry Core Unit, Max Planck Institute for Molecular Genetics, Berlin, Germany, ⁹German Center for Diabetes Research (DZD), München-Neuherberg, Germany, ¹⁰Institute of Nutritional Science, University of Potsdam, Potsdam, Germany

Abstract

Background Neurofibromatosis type 1 (NF1) is a multi-organ disease caused by mutations in neurofibromin 1 (*NF1*). Amongst other features, NF1 patients frequently show reduced muscle mass and strength, impairing patients' mobility and increasing the risk of fall. The role of Nf1 in muscle and the cause for the NF1-associated myopathy are mostly unknown.

Methods To dissect the function of *Nf1* in muscle, we created muscle-specific knockout mouse models for NF1, inactivating *Nf1* in the prenatal myogenic lineage either under the Lbx1 promoter or under the Myf5 promoter. Mice were analysed during prenatal and postnatal myogenesis and muscle growth.

Results Nf1^{Lbx1} and Nf1^{Myf5} animals showed only mild defects in prenatal myogenesis. Nf1^{Lbx1} animals were perinatally lethal, while Nf1^{Myf5} animals survived only up to approximately 25 weeks. A comprehensive phenotypic characterization of Nf1^{Myf5} animals showed decreased postnatal growth, reduced muscle size, and fast fibre atrophy. Proteome and transcriptome analyses of muscle tissue indicated decreased protein synthesis and increased proteasomal degradation, and decreased glycolytic and increased oxidative activity in muscle tissue. High-resolution respirometry confirmed enhanced oxidative metabolism in Nf1^{Myf5} muscles, which was concomitant to a fibre type shift from type 2B to type 2A and type 1. Moreover, Nf1^{Myf5} muscles showed hallmarks of decreased activation of mTORC1 and increased expression of atrogenes. Remarkably, loss of Nf1 promoted a robust activation of AMPK with a gene expression profile indicative of increased fatty acid catabolism. Additionally, we observed a strong induction of genes encoding catabolic cytokines in muscle Nf1^{Myf5} animals, in line with a drastic reduction of white, but not brown adipose tissue.

Conclusions Our results demonstrate a cell autonomous role for Nf1 in myogenic cells during postnatal muscle growth required for metabolic and proteostatic homeostasis. Furthermore, Nf1 deficiency in muscle drives cross-tissue communication and mobilization of lipid reserves.

Keywords Neurofibromatosis / NF1; Myopathy; Muscle atrophy; Muscle metabolism; Muscle fibre type; AMPK

Received: 2 April 2020; Revised: 9 July 2020; Accepted: 10 September 2020

*Correspondence to: Sigmar Stricker, Institut für Chemie und Biochemie, Freie Universität Berlin, Thielallee 63, 14195 Berlin, Germany. Phone: +49 30 838 75799, Fax: +49 30 838 475799, Email: sigmar.stricker@fu-berlin.de

Introduction

Neurofibromatosis type 1 (NF1) is a multi-organ disease caused by mutations in the *NF1* gene. *NF1* encodes a Ras-GTPase-activating protein, neurofibromin 1, which negatively regulates Ras signalling, mainly feeding into the MAPK pathway, specifically Mek1/2–Erk1/2 signalling, depending on the cell type. In contrast, other pathways were shown to be activated, such as cAMP in Schwann cells, or PI3Kinase/AKT in astrocytes and malignant peripheral nerve sheath tumours.¹ The musculoskeletal system is often affected in NF1 patients, with scoliosis, long bone dysplasia, and osteoporosis being a main cause of considerable morbidity.² Furthermore, pronounced reduction of muscle size and muscle weakness has been reported in NF1 patients^{3–8} and has also been described as general feature in RASopathies, that is, disease traits with mutations in RAS pathway components.^{9,10} However, the cause of muscle weakness is unknown.

Skeletal muscles consist of syncytial multinucleated myofibres that produce force based on the activity of contractile proteins. During postnatal growth, myofibres continuously increase their size by myonuclear accretion and protein synthesis, mainly components of the contractile machinery, in a process termed hypertrophy.^{11,12} Myofibres are generally classified into slow-twitching type 1 and fast-twitching type 2 fibres that differ in the expression of specific myosin heavy chain isoforms as well as their metabolic profile. While slow-twitching fibres mainly rely on oxidative metabolism based on carbohydrates and fatty acids, fast-twitching fibres are further divided into fast oxidative (type 2A) or fast glycolytic (type 2B and 2X in mice, 2X in humans) fibres.^{13–15} Myopathies affect the functionality of muscle fibres, by, for example, perturbing the function of contractile proteins or the integrity of the myofibre, or by changes in protein turnover leading to net protein loss and myofibre atrophy. Thereby, fibre types can be differentially affected, for example, in Duchenne muscular dystrophy or in age-related sarcopenia; predominantly, fast glycolytic fibres are most prone to atrophy.^{15,16}

During development, skeletal muscles of the trunk arise from the somitic mesoderm. The muscles of the limbs instead originate from the ventrolateral lip of the dermomyotome, where cells detach and migrate into the limb buds, where they invade the resident mesenchyme. There, cells start to induce a cascade of so-called myogenic regulatory factors (Myf5, Myf6/Mrf4, MyoD, and myogenin) that consecutively specify and consolidate myogenic commitment and differentiation. Inactivation of *Nf1* in limb mesenchyme during development using *Prx1*^{Cre} recapitulated the skeletal manifestations of NF1^{17,18} but also caused an early-onset defect in embryonal myogenesis,¹⁹ providing the first evidence for a direct involvement of *Nf1* in myogenesis. Postnatally, *Nf1*^{Prx1} mice recapitulated NF1 features as muscle weakness and fibro-fatty infiltration of muscle.^{19,20} However, in this model,

Nf1 is inactivated in the skeleton as well as in the accessory tissues of muscles (tendons and connective tissue).^{19,21} Inactivation of *Nf1* in the myogenic lineage using *MyoD*^{Cre} resulted in early postnatal lethality²² limiting the utility of this model for postnatal analysis.

Here, we use *Lbx1*^{Cre} and *Myf5*^{Cre} to delete *Nf1* in the myogenic lineage. *Lbx1*^{Cre} leads to inactivation in early migrating progenitors, while *Myf5*^{Cre} leads to inactivation in committed myoblasts. While *Lbx1*^{Cre}-mediated inactivation of *Nf1* led to perinatal lethality, inactivation of *Nf1* via *Myf5*^{Cre} provided viable offspring and allowed postnatal analysis. We show that loss of *Nf1* in the myogenic lineage compromises postnatal muscle growth resulting in severely reduced muscle size caused by decreased mTORC1 signalling activity. Moreover, *Nf1*-deficient muscle shows a glycolytic-to-oxidative fibre type shift concomitant to decreased carbohydrate but increased lipid metabolism and attrition of white adipose tissue (WAT). This demonstrates a cell autonomous requirement for *Nf1* in the myogenic lineage and provides a mechanistic explanation for NF1-associated muscle weakness.

Methods

Animals

Mouse lines used in this study were described before: *Myf5*^{Cre,23}, *Lbx1*^{Cre,24}, *Nf1*^{flox,25} and *Rosa26*^{mTmG,26}. All animal procedures conducted within this study have been approved by the appropriate ethics committee and have therefore been performed in accordance with the ethical standards laid down in the 1964 Declaration of Helsinki and its later amendments. Animal studies were conducted in accordance with FELASA guidelines and were approved by the responsible authority (Landesamt für Gesundheit und Soziales Berlin, LAGeSo) under license numbers ZH120, G0346/13, and G0176/19. Timed matings were set up, and mice were sacrificed by cervical dislocation at indicated days of pregnancy; foetuses were sacrificed by decapitation.

Tissue processing and histology

Forelimbs and hindlimbs of mice were dissected, limbs from the right side of the body were embedded in paraffin, and limbs from the other side were snap-frozen in liquid nitrogen, followed by RNA, gDNA, or protein isolation. Adipose tissue was taken for RNA isolation and paraffin embedding. Muscle tissue was embedded with tragacanth (Sigma-Aldrich #G1128) on a cork plate into cold isopentane for 10 s; then samples were transferred on dry ice and stored at -80°C . Adipose tissue was embedded with paraffin after using PFA fixation and rounds of dehydration. Cryoembedded samples were sectioned using a microtome (Microm HM355S) with a

thickness of 10 μm . For immunostaining, slides were fixed with methanol for 10 min at -20°C . Antigen retrieval was used for Pax7 staining with antigen retrieval solution (2 mM EDTA) for 10 min at 95°C water bath (Julabo). Slides were blocked with blocking buffer (5% BSA in PBX) for 1 h at room temperature. Primary antibodies were diluted with blocking buffer and incubated overnight at 4°C . To remove primary antibody, slides were washed four times 10 min each with PBX. Secondary antibody was applied in PBX for 1 h at room temperature followed by washing with PBX for four times. Slides were mounted with Fluoromount-G (Southern Biotech, #0100-01). Imaging was performed on a LSM700 confocal microscope (Zeiss) with ZEN imaging software (Zeiss). The primary antibodies and dilutions used were goat anti-collagen IV (Millipore AB769; 1:500), mouse anti-MyHC type 1 (DSHB BA-D5; 1:500), mouse anti-MyHC type 2A (DSHB SC-71; 1:200), rabbit anti-laminin (Sigma-Aldrich L9393; 1:500), mouse anti-Pax7 (DSHB Pax7; 1:10), mouse anti-myosin heavy chain (Sigma-Aldrich 05-716; 1:1000), anti-beta III tubulin antibody (Sigma-Aldrich AB9354; 1:500), and anti-perilipin A/B antibody (Sigma-Aldrich p1873; 1:250). For all the immunostaining analysis, three to five animals were used for each genotype as indicated in the figure legends.

Paraffin embedding of adipose tissue from control ($n = 3$) and Nf1^{Myf5} ($n = 3$) animals were used for haematoxylin and eosin staining; slides were fixed with 4% PFA at room temperature for 10 min and then incubated with haematoxylin (Carl Roth 3816) for 1 min, followed by eosin (Sigma Aldrich #15086-94-9) staining for 30 s. Slides were dehydrated by incubation for 5 min each in 70% EtOH–80% EtOH–90% EtOH–100% EtOH–xylene (Carl Roth #CN80). Slides were mounted with Permount medium (Science Service E17986).

Oil Red O staining was performed with control ($n = 3$) and Nf1^{Myf5} ($n = 3$) muscle sections from different development stages; slides were rinsed with 60% isopropanol (Carl Roth 6752) for 10 min followed by incubation with Oil Red O (Sigma Aldrich O0625) staining solution (0.5 g Oil Red O in 100 mL isopropanol) for 15 min. Then slides were rinsed with 60% isopropanol for 10 min and washed with PBS before mounting and imaging.

Quantitative RT–PCR

Total RNA was isolated with RNeasy Micro Kit or RNeasy Mini Kit (Qiagen). cDNA was synthesized using 1 μg of mRNA with SuperScript[™] III Reverse Transcriptase (Invitrogen 18080044), Oligo(dT)20 Primer (Invitrogen 18418020), and RNaseOUT Recombinant Ribonuclease Inhibitor (ThermoFisher Scientific 10777019) according to the protocol provided by the manufacturers. In brief, 1:10 cDNA dilution was used for each reaction of quantitative RT–PCR analysis performed on an ABI Prism HT 7900 real-time PCR detection system (Applied Biosystems) equipped with SDS software version 2.4

(ThermoFisher Scientific) using GoTaq qPCR Master Mix (Promega) or SYBR Green qPCR Master Mix (Life Technologies). Beta-actin was used to normalize the expression of each gene. All primers used were purchased from Eurofins Scientific and are listed in the Supporting Information, *Table S1*. For all assays, samples from three to four animals per genotype were used in three technical replicates.

RNA sequencing analysis

Total RNA was isolated from tibialis anterior (TA) muscles of two $\text{p21 Myf5}^{\text{Cre}};\text{Nf1}^{\text{flox/+}}$ and two $\text{p21 Myf5}^{\text{Cre}};\text{Nf1}^{\text{flox/flox}}$ animals using RNeasy Micro Kit or RNeasy Mini Kit (Qiagen). After initial quality control using Agilent Bioanalyzer, sequencing libraries were prepared from 500 ng of total RNA per sample following Roche's 'KAPA stranded mRNA Seq' library preparation protocol for single indexed Illumina libraries: first, the polyA-RNA fraction was enriched using oligo-dT-probed paramagnetic beads. Enriched RNA was heat fragmented and subjected to first-strand synthesis using random priming. The second strand was synthesized incorporating dUTP instead of dTTP to preserve strand information. After A-tailing Illumina sequencing compatible adapters were ligated. Following bead-based clean-up steps, the libraries were amplified using 11 cycles of PCR. Library quality and size was checked with qBit, Agilent Bioanalyzer, and qPCR. Sequencing was carried out on an Illumina HiSeq 4000 system in PE75bp mode yielding between 45 and 72 million fragments per sample. Mapping was performed using STAR 2.4.2a software with mouse genome (mm9). Read counts were generated with R Studio function Summarize Overlaps and normalized to RPKM based on the number of uniquely mapped reads. Differential expression analysis was performed with DESeq2 using default settings. Genes with an absolute fold change > 2 and adjusted P -value < 0.01 were assessed to be significantly differentially expressed. A table of DESeq2 analysis can be found in the Supporting Information, *Data S1*. Gene set enrichment analysis (GSEA) was performed with the entire gene list using GSEA software 4.0.1 desktop (Broad Institute). KEGG and gene ontology (GO) enrichment analysis was performed using the Signature Database (MSigDB) and DAVID 6.8. RNA-seq data have been deposited in the Gene Expression Omnibus database under the SuperSeries accession number GSE147605.

Immunoblotting

For protein isolation, tissue homogenization was performed with a TissueLyser (Qiagen) with RIPA buffer (50 mM Tris–HCl, pH 8.0; 150 mM NaCl; 1% NP-40; 0.5% sodium deoxycholate; 0.1% SDS). Protein concentration was measured with the Pierce BCA Protein Assay Kit (Thermo Fisher

#23225). Protein concentration from all samples was adjusted to 1.5 or 3 $\mu\text{g}/\mu\text{L}$. Total protein (30 μg) was separated with SDS-PAGE gels and transferred to PVDF membrane (GE Healthcare). Membranes were blocked with 5% BSA in TBST for 1 h at room temperature. Primary antibodies were diluted in blocking buffer and applied overnight at 4°C. Antibodies used were rabbit anti-PPARG (Cell Signaling Technology 2443), rabbit anti-phosphor (pThr172) AMPK α (Cell Signaling Technology 2535), rabbit anti-AMPK α (Cell Signaling Technology 2532), mouse anti- β -actin (Cell Signaling Technology 58169), mouse anti- β -tubulin (Sigma-Aldrich T8328), rabbit anti-phosphor (s235/236) S6 (Cell Signaling Technology 4858), mouse anti-MyHC type 1 (DSHB BA-D5), mouse anti-MyHC type 2B (DSHB BF-F3), rabbit anti-phosphor (Ser473) AKT (Cell Signaling, #9271; 1:1000), rabbit anti-phospho (Ser1101) IRS-1 (Cell Signaling, #2385; 1:1000), and rabbit anti-phospho (Ser636/639) IRS-1 (Cell Signaling, #2388; 1:1000). Secondary antibodies were applied for 1 h at room temperature. Antibodies used were IgG (HRP conjugated) anti-rabbit (Thermo Fisher; 1:1000) and IgG (HRP conjugated) anti-mouse (Thermo Fisher; 1:1000). Images were acquired using a Fusion FX spectra gel documentation system (Vilber) with FUSION FX software. Blots images were analysed with ImageJ grey value analysis tool. For quantification, samples from at least three animals per genotype were analysed in at least three technical replicates.

Proteomics sample preparation

Three biological replicates of Nf1^{Myf5} and control (Nf1^{fllox/+}; Myf5^{Cre} and Nf1^{+/+}; Myf5^{Cre}) TA muscles from p21 mice were used for proteome profiling. Proteomics sample preparation was performed according to a published protocol with minor modifications.²⁷ In brief, about 10 mg frozen tissue per sample were homogenized under denaturing conditions with a FastPrep (two times for 60 s, 4 m/s) in 1 mL of a buffer containing 6 M guanidinium chloride (GdmCl), 5 mM tris(2-carboxyethyl)phosphine, 20 mM chloroacetamide, and 50 mM Tris-HCl pH 8.5. Lysates were boiled at 95°C for 15 min in a thermal shaker, followed by sonication for 15 min, and centrifuged at 15 000 *g* for 5 min. The supernatant was transferred into new protein low binding tubes (Eppendorf, Germany). One hundred micrograms of protein per sample were diluted to 1 M GdmCl by adding 10% acetonitrile and 25 mM Tris, 8.5 pH, followed by a Lys-C digestion (1:50) at 37°C for 2 h. This was followed by another dilution to 0.5 M GdmCl and a tryptic digestion (1:50) at 37°C overnight. Subsequently, peptides were desalted with C18 columns and reconstituted in 1% formic acid in water and further separated into five fractions by strong cation exchange chromatography (SCX, 3M Purification, Meriden, CT). Eluates were first dried in a SpeedVac, then dissolved in 20 μL 5% acetonitrile and 2% formic acid in water, briefly

vortexed, and sonicated in a water bath for 30 s prior injection to nano-LC-MS/MS. Five micrograms of each SCX fraction and a non-fractionated sample were used for proteome profiling and analysed by MaxQuant (v1.5.3.30).

LC-MS/MS instrument settings for shotgun proteome profiling with label-free quantification and data analysis

LC-MS/MS was carried out by nanoflow reverse phase liquid chromatography (Dionex Ultimate 3000, Thermo Scientific) coupled online to a Q-Exactive HF Orbitrap mass spectrometer (Thermo Scientific), as reported previously.²⁸ Briefly, the LC separation was performed using a PicoFrit analytical column (75 μm ID \times 50 cm long, 15 μm Tip ID; New Objectives, Woburn, MA) in-house packed with 3 μm C18 resin (Reposil-AQ Pur, Dr. Maisch, Ammerbuch, Germany). Peptides were eluted using a gradient from 3.8 to 38% solvent B in solvent A over 120 min at 266 nL/min flow rate. Solvent A was 0.1% formic acid, and solvent B was 79.9% acetonitrile, 20% H₂O, and 0.1% formic acid. Nano-electrospray was generated by applying 3.5 kV. A cycle of one full Fourier transformation scan mass spectrum (300–1750 *m/z*, resolution of 60 000 at *m/z* 200, automatic gain control target 1×10^6) was followed by 12 data-dependent MS/MS scans (resolution of 30 000, automatic gain control target 5×10^5) with a normalized collision energy of 25 eV. In order to avoid repeated sequencing of the same peptides, a dynamic exclusion window of 30 s was used. In addition, only peptide charge states between two and eight were sequenced.

Raw MS data were processed with MaxQuant software (v1.5.3.30) and searched against the mouse proteome database UniProtKB (UP000000589) with 54 416 entries, released in March 2016. Parameters of MaxQuant database searching were a false discovery rate (FDR) of 0.01 for proteins and peptides, a minimum peptide length of seven amino acids, a first search mass tolerance for peptides of 20 ppm, and a main search tolerance of 4.5 ppm. A maximum of two missed cleavages was allowed for the tryptic digest. Cysteine carbamidomethylation was set as fixed modification, while N-terminal acetylation and methionine oxidation were set as variable modifications. The label-free quantification algorithm, implemented in MaxQuant, was used for data normalization. The MaxQuant processed output files can be found in the Supporting Information, *Data S2*, showing peptide and protein identification, accession numbers, % sequence coverage of the protein, *q*-values, and label-free quantification intensities. The mass spectrometry data have been deposited to the ProteomeXchange Consortium (<http://proteomecentral.proteomexchange.org>) via the PRIDE partner repository²⁹ with the dataset identifier PXD017958.

Statistical analysis was performed by a two-sample *t*-test with Benjamini-Hochberg (FDR of 0.05) correction for

multiple testing. Significantly regulated proteins between Nf1^{Myf5} and controls were indicated in the Supporting Information, *Data S3*, and were submitted to DAVID bioinformatics 6.8 for functional annotation analysis. For comprehensive proteome data analyses, GSEA (v2.2.3)³⁰ was applied in order to see if a priori defined sets of proteins show statistically significant, concordant differences between Nf1^{Myf5} and controls. GSEA standard settings were used, except that the minimum size exclusion was set to 5 and KEGG v5.2 were used as gene set databases. The cut-off for significantly regulated pathways was set to be ≤ 0.05 *P*-value and ≤ 0.05 FDR.

High-resolution respirometry

Extensor digitorum longus (EDL) and soleus muscles from 5 weeks control ($n = 7$) and Nf1^{Myf5} ($n = 7$) mice were used in this experiment. Briefly, gently dissected muscles were put into ice-cold biopsy preservation medium (in mM: 2.77 CaK₂EGTA, 7.23 K₂EGTA, 20 imidazole, 20 taurine, 6.56 MgCl₂, 5.77 ATP, 3.95 phosphocreatine, 0.5 dithiothreitol, 50 K-MES, pH 7.1 at °C) followed by permeabilization with saponin (50 µg/mL) in biopsy preservation medium at 4°C for 30 min. Fibres were washed with mitochondrial respiration medium (MiRO5, 110 mM sucrose, 60 mM K-lactobionate, 0.5 mM EGTA, 3 mM MgCl₂, 20 mM taurine, 10 mM KH₂PO₄, 20 mM HEPES, pH 7.1, and 0.1% fatty acid-free BSA) at 4°C for 10 min. All samples were kept on ice before analysis. The basic principle of this method is to analyse the respiratory capacity at 37°C in a hyperoxygenated environment using a multiple substrate-uncoupler-inhibitor titration protocol.³¹ The following concentrations were used: 2 mM malate + 5 mM pyruvate (LEAK respiration), 5 mM ADP (OXPHOS capacity), 10 µM cytochrome c (integrity of outer mt-membrane), 10 mM glutamate (OXPHOS capacity), 10 mM succinate (OXPHOS capacity), 0.5 µM FCCP (ETS capacity, ETSCI&CII), 0.5 µM rotenone (ETS capacity, ETSCII), and 2.5 µM antimycin A (residual oxygen consumption, ROX) that were used with high-resolution Oxygraph-2k (OROBOROS Instruments). DatLab software (OROBOROS INSTRUMENTS) was used for data acquisition and analysis. All data were normalized to non-mitochondrial residual oxygen consumption (after complex I and III inhibition by adding rotenone and antimycin A) and muscle fibre wet weight. Student's *t*-test (unpaired, two-tailed) was used to determine differences between genotypes for each respiratory state.

Whole mount in situ hybridization

Embryos at the stage E14.5 were dissected and fixed overnight in 4% PFA/PBS. Embryos were washed twice in PBST for 30 min on ice and dehydrated through 25%, 50%, and 75% methanol in PBST (DEPC-H₂O), twice in 100% methanol

for 10 min, and were stored in methanol at -20°C. Embryos were rehydrated passing through 75%, 50%, and 25% methanol in PBST (DEPC-H₂O) and washed twice with 1× PBS (DEPC-H₂O) on ice. Afterwards, embryos were bleached with 6% hydrogen peroxide in PBST for 1 h on ice. After washing three times for 10 min in PBST, embryos were treated with proteinase K (20 µg/mL, Roche) at room temperature for 12 min. Embryos were washed with PBST, PBST/glycine, and RIPA buffer for 10 min each and fixed with 4% PFA/0.2% glutaraldehyde for 20 min followed by washing with PBST, PBST/hybridization buffer, and hybridization buffer (50% formamide, 5× SSC pH 4.5, 1% SDS and 0.1% Tween-20, 0.1 mg/mL tRNA, and 0.05 mg/mL heparin). Embryos were pre-hybridized in hybridization solution at 65°C for 3 h, followed by incubation in hybridization buffer containing a digoxigenin-labelled *MyoD* mRNA probe at 65°C overnight. Embryos were washed with hybridization buffer at 65°C for 30 min, followed by digestion with RNase A at 37°C for 30 min. Embryos were washed with formamide buffer (50% formamide, 2× SSC pH 4.5, 0.1% Tween-20 in DEPC-water) at 65°C for 30 min, followed by two washing steps with MABT for 15 min each. Embryos were incubated in blocking solution (2% foetal calf serum, 2 mg/mL bovine serum albumin dissolved in TBST) for 1 h and subsequently incubated with anti-DIG-Fab antibody coupled to alkaline phosphatase (Roche, 11093274910) in blocking solution (1 in 5000) at 4°C overnight. Embryos were washed with PBST/tetramisol overnight. Embryos were equilibrated to ALP buffer for three times, 20 min each, and then transferred to BM purple AP substrate (Roche, 11442074001). For signal conservation, the embryos were washed three times with ALP buffer and then fixed in 4% PFA/PBS. Imaging was performed using a Zeiss Stereo Discovery V12 and the AxioVision 4.6 software (Zeiss). Measurement and quantification of MyoD⁺ stained area were performed on three embryos for each genotype with the Autmess function of AxioVision 4.6.

Results

Conditional inactivation of Nf1 in myogenic progenitors causes reduction of postnatal muscle growth

To specifically inactivate *Nf1* in the myogenic lineage, we used the Lbx1^{Cre24} and Myf5^{Cre23} lines, targeting migrating and early committed myogenic progenitors, respectively. Both lines were reanalysed for their specific activity in the myogenic lineage (Supporting Information, *Figure S1A* and *S1B*). In the limbs, Lbx1^{Cre} and Myf5^{Cre} were highly specific to the myogenic lineage and did not cause reporter recombination in, for example, neural cells, connective tissue, or cartilage. The Myf5^{Cre} line showed minimal off-target activity in

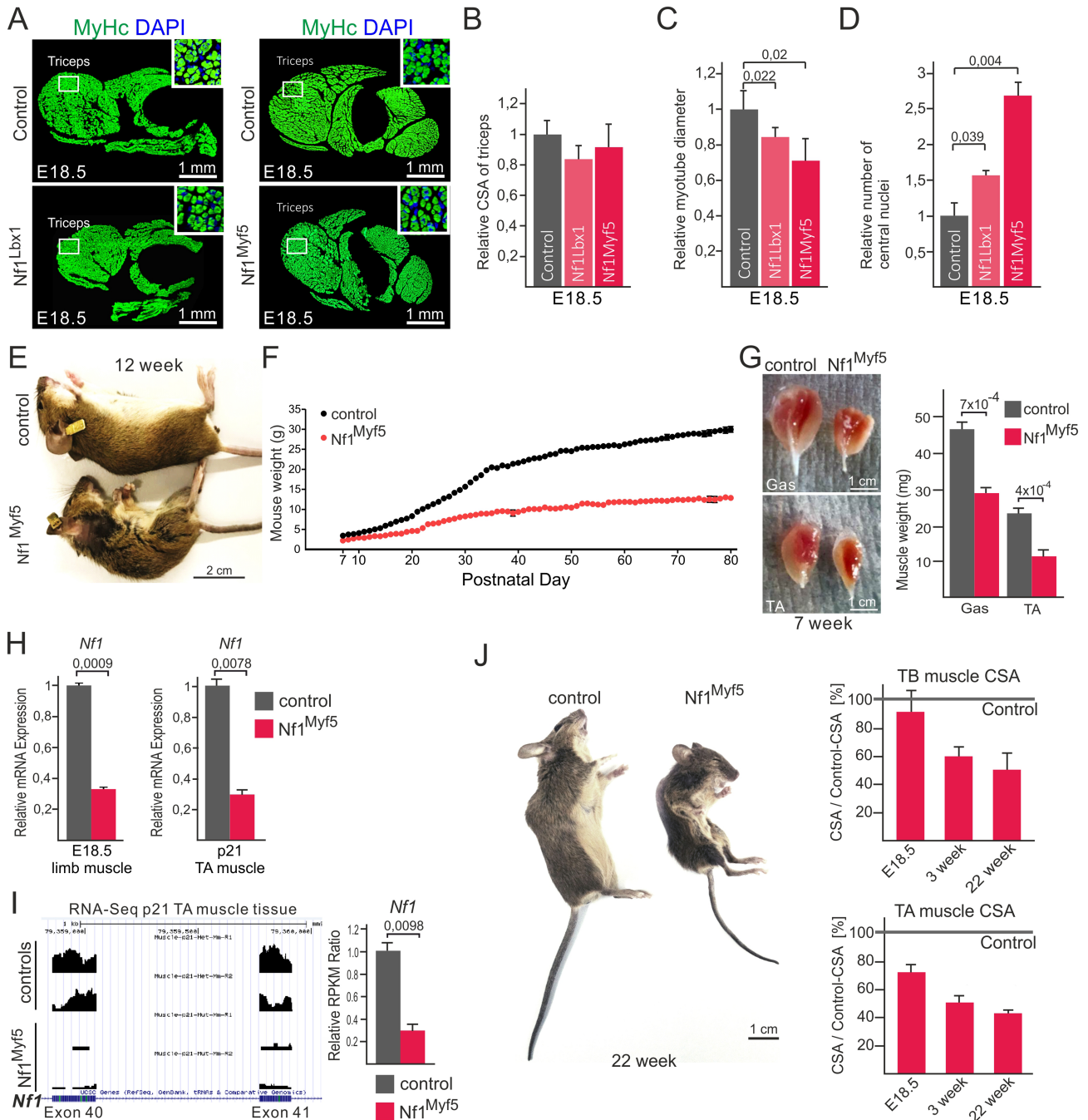


FIGURE 1 Muscle-specific inactivation of *Nf1* causes reduced postnatal muscle growth. (A) Forelimb cross sections of control, Nf1^{Lbx1}, and Nf1^{Myf5} E18.5 fetuses stained for pan-MyHC. Triceps brachii (TB) muscle is indicated; squared region is shown as magnification in inserts. (B) Quantification of TB cross-sectional area (CSA) of E18.5 controls, Nf1^{Lbx1}, and Nf1^{Myf5} animals. (C) Quantification of myotube diameter in TB muscles of E18.5 controls, Nf1^{Lbx1}, and Nf1^{Myf5} animals. (D) Quantification of number of centrally located nuclei in TB muscles of E18.5 controls, Nf1^{Lbx1}, and Nf1^{Myf5} animals. (B–D: $n = 3$ animals per genotype). (E) Control and Nf1^{Myf5} mice at 12 weeks of age. (F) Weight curve of control (black) and Nf1^{Myf5} (red) animals during postnatal life starting at postnatal day 7 ($n = 4$ animals per genotype; $P < 0.001$; two-way analysis of variance with Bonferroni post-test). (G) Dissected gastrocnemius (Gas) and tibialis anterior (TA) muscles of control and Nf1^{Myf5} animals at 7 weeks of age. Quantification is shown right ($n = 3$ animals per genotype). (H) RT-qPCR analysis of *Nf1* deletion efficacy in E18.5 or p21 muscle tissue from control vs. Nf1^{Myf5} mice ($n = 3$ animals per genotype). (I) RNA-Seq tracks showing coverage of *Nf1* exons 40 and 41 in control and Nf1^{Myf5} mice. Quantification is shown right (RPKM, reads per kilobase million). (J) Appearance of 22-week-old control and Nf1^{Myf5} animals. Right: TB and TA CSA of E18.5, p21, and 22-week-old Nf1^{Myf5} animals are depicted relative to controls, which was set as 100% (horizontal line) ($n = 3$ animals per genotype). Error bars represent standard error of means. P -value was calculated by two-sided unpaired t -test except for (F).

dorsal root ganglia, as described previously,²³ but no recombination was detected in limb neurons (Supporting Information, Figure S1A and S1B). Unlike inactivation of *Nf1* in limb mesenchyme using *Prx1^{Cre}*,¹⁹ inactivation in the myogenic lineage did not cause a marked defect in early myogenesis at embryonal day (E) 14.5 (Supporting Information, Figure S2A). In late foetal development (E18.5) in both lines, myofibre cross-sectional areas were unaltered, while myofibre diameters tended to be decreased, and numbers of central myonuclei were increased (Figure 1A–1D), indicating a slight developmental delay. Newborn *Lbx1^{Cre};Nf1^{flox/flox}* mice were smaller, exhibited cyanosis and lack of feeding, and died perinatally. *Myf5^{Cre};Nf1^{flox/flox}* mice were born at normal Mendelian ratios at normal size and were used for further analysis. *Myf5^{Cre};Nf1^{flox/flox}* mice are further on termed '*Nf1^{Myf5}*'. *Myf5^{Cre};Nf1^{flox/+}* mice were indistinguishable from *Nf1^{+/+}* mice and had equal *Nf1* mRNA expression levels (Supporting Information, Figure S2B) and were therefore used as controls unless otherwise noted. Postnatally, *Nf1^{Myf5}* mice showed a marked growth retardation and

weight reduction (Figure 1E and 1F). Dissection of individual muscles (gastrocnemius and tibialis anterior, TA) showed significantly decreased muscle size (Figure 1G) compared with control littermates at 7 weeks of age. Efficacy of *Nf1* deletion was controlled in E18 and p21 muscle tissue (Figure 1H and 1I). Note that, although the *Myf5^{Cre}* allele is a loss of function, *Myf5* mRNA expression in whole muscle tissue both during development (E18.5) and at p21 was indistinguishable between *Myf5^{+/+}* and *Myf5^{Cre/+}* mice (Supporting Information, Figure S2C), indicating compensation by the intact allele. The reduction in muscle size was observed throughout lifespan (Figure 1J), which for *Nf1^{Myf5}* mice consistently was approximately 20–25 weeks. Together, this suggests a defect in postnatal muscle growth.

Fast fibre atrophy of *Nf1^{Myf5}* muscles

We next analysed muscles of young mice amidst the most intense phase of muscle growth, at 3 weeks of age (p21) by

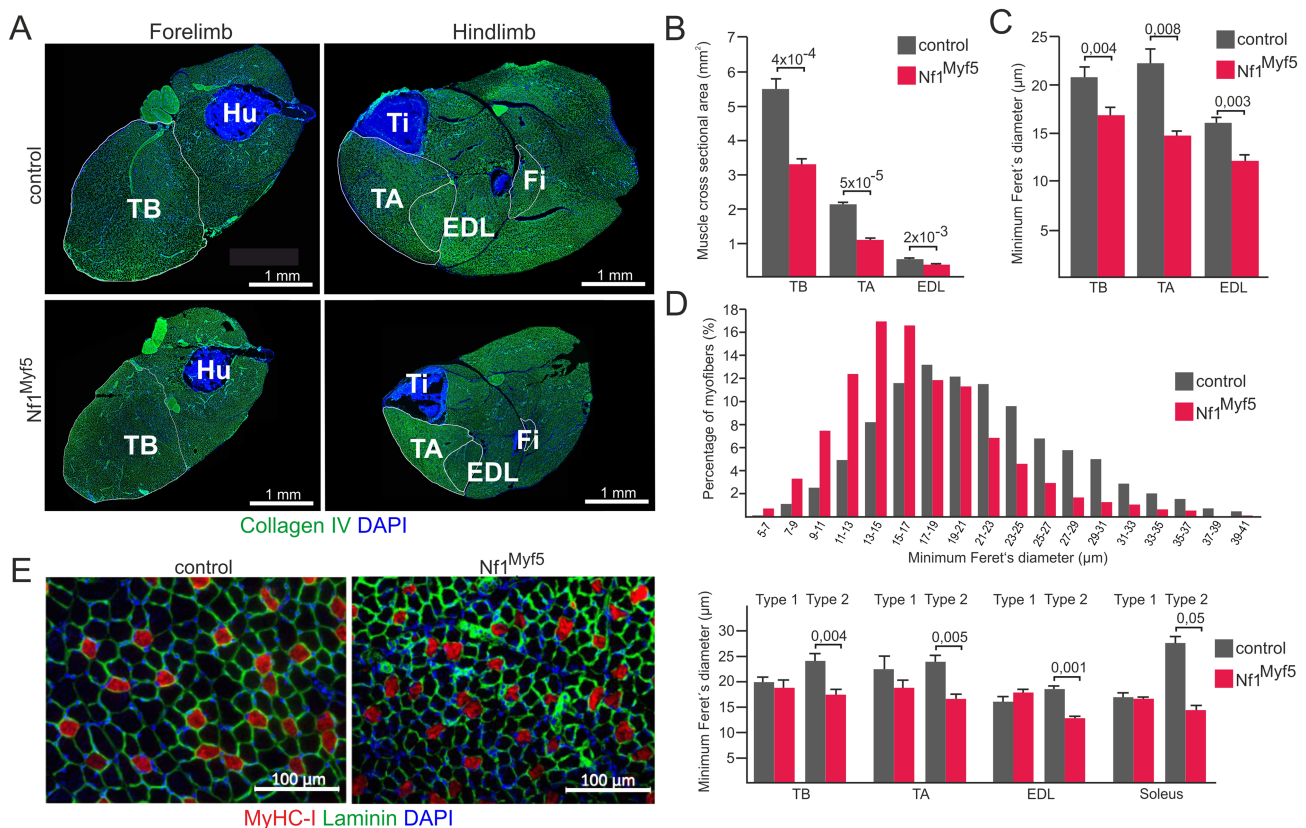


FIGURE 2 Muscle-specific inactivation of *Nf1* causes fast fibre atrophy. (A) Cross sections of forelimb and hindlimb of control and *Nf1^{Myf5}* animals. Staining: collagen IV (green), DAPI (blue). EDL, extensor digitorum longus; Fi, fibula; Hu, humerus; TA, tibialis anterior; TB, triceps brachii; Ti, Tibia. (B) Quantification of the cross-sectional area of muscles indicated [$n = 4$ (controls), $n = 5$ (*Nf1^{Myf5}*)]. (C) Quantification of minimum Feret's diameter of individual muscle fibres on tissue cross sections of muscles indicated [$n = 4$ (controls), $n = 5$ (*Nf1^{Myf5}*)]. (D) Distribution of myofiber diameter in control and *Nf1^{Myf5}* animals [$n = 4$ (controls), $n = 5$ (*Nf1^{Myf5}*)]. (E) Cross section of TA muscles of control and *Nf1^{Myf5}* animals. Staining: myosin heavy chain type 1 (red), laminin (green), DAPI (blue). Quantification of diameters of type 1 vs. type 2 myofibers is shown right [$n = 3$ (controls), $n = 4$ (*Nf1^{Myf5}*)]. Error bars represent standard error of means. *P*-value was calculated by two-sided unpaired *t*-test.

histology. Muscles in forelimb and hindlimb [triceps brachii (TB), tibialis anterior (TA), and extensor digitorum longus (EDL)] showed reduced cross-sectional area (Figure 2A and 2B). Centrally located myonuclei were not observed in muscles of p21 or 12-week-old $Nf1^{Myf5}$ mice (not shown). Myofibre numbers were not significantly altered in all three muscles (Supporting Information, Figure S2D). Conversely, myofibre diameter was reduced in TB, TA, and EDL of $Nf1^{Myf5}$ mice (Figure 2C). This was confirmed by binning fibre diameters of TB, TA, and EDL into discrete size windows, demonstrating global shift towards smaller fibres in $Nf1^{Myf5}$ mice (Figure 2D). Staining for type 1 fibres (MyHC-1⁺) revealed a predominant size reduction of type 2 muscle fibres (Figure 2E). We conclude that $Nf1^{Myf5}$ mice show impaired postnatal myofibre growth and persistent fast myofibre atrophy.

Proteome and transcriptome analyses of $Nf1^{Myf5}$ muscles

To assess global changes in $Nf1$ -deficient muscle tissue, we performed proteome as well as transcriptome analysis of whole TA muscles at p21. Note that for the proteome analysis we used both $Myf5^{Wt};Nf1^{lox/+}$ and $Myf5^{Cre};Nf1^{lox/+}$ muscle tissues as controls. Principal component analysis showed that both control genotypes were grouped together, while $Nf1^{Myf5}$ samples were grouped separately (Supporting Information, Figure S3A). This demonstrates that, at least on the proteome level, influence of the $Myf5^{Cre}$ allele (i.e. haploinsufficiency for $Myf5$), as well as $Nf1$ haploinsufficiency, can be neglected. Proteome analysis of p21 TA muscle lysates yielded 274 significantly deregulated proteins between controls and $Nf1^{Myf5}$ (Figure 3A). KEGG pathway analysis showed enrichment for the categories 'translation', 'carbon metabolism', and 'ribosome' amongst proteins down-regulated in $Nf1^{Myf5}$ mutants compared with controls (Figure 3B). Amongst proteins up-regulated in $Nf1^{Myf5}$ muscle, KEGG terms 'oxidative phosphorylation', 'protein digestion', 'proteasome', 'PPAR signaling pathway', and 'fatty acid degradation' were overrepresented (Figure 3B).

This was confirmed by RNA-Seq analysis of p21 TA muscle tissue. Principal component analysis confirmed separate clustering of control and $Nf1^{Myf5}$ samples (Supporting Information, Figure S3B). Transcriptome analysis yielded 1917 differentially expressed genes; 928 genes were down-regulated and 989 genes were up-regulated in $Nf1^{Myf5}$ muscle relative to controls (Figure 3C). GO as well as KEGG analysis of transcriptome data highlighted terms as 'muscle cell differentiation', 'muscle hypertrophy', 'carbohydrate metabolism' or 'glycolysis/gluconeogenesis' as overrepresented in genes down-regulated in $Nf1^{Myf5}$ muscle (Figure 3D). Conversely, terms as 'oxidation-reduction process', 'mitochondrial electron transport chain', 'TCA cycle', or

'oxidative phosphorylation', as well as several terms related to amino acid catabolism, were enriched in genes up-regulated in $Nf1^{Myf5}$ muscle (Figure 3E). We note that, although affected biological processes align between proteome and transcriptome analyses, deregulated proteins and genes [including tricarboxic acid (TCA) cycle and OXPHOS] are not positively correlated (Supporting Information, Figure S3C). While under steady-state conditions mRNA and protein levels typically correlate, discrepancy is not uncommon for dynamic situations,³² which we consider the case for our $Nf1^{Myf5}$ mutant. We also noted 'insulin signaling pathway' enriched in down-regulated genes; we therefore first analysed $Nf1^{Myf5}$ mice for blood glucose levels, which were unchanged (Supporting Information, Figure S4A). Also, phosphorylation of Akt as well as IRS1 in random fed animals was not significantly changed (Supporting Information, Figure S4B and S4C). In summary, proteome and transcriptome analyses suggest (i) metabolic shift and (ii) deranged protein homeostasis in $Nf1^{Myf5}$ mice.

Increased oxidative metabolism in $Nf1^{Myf5}$ muscle

Skeletal muscle primarily gains energy by breakdown of carbohydrates and fatty acids, both being able to feed into mitochondrial respiration as the most efficient way of ATP production. In $Nf1^{Myf5}$ muscle, GO as well as KEGG categories associated with the TCA cycle or the mitochondrial electron transport chain were overrepresented in genes and proteins up-regulated in $Nf1^{Myf5}$ muscle (Figure 3B and 3E). GSEA of the RNA-Seq data highlighted enrichment of genes associated with 'glucose catabolic process' in control muscle and of genes associated with 'oxidative phosphorylation' in $Nf1^{Myf5}$ muscle (Figure 4A). We therefore mined the differentially expressed gene set for genes encoding components of glycolysis or TCA cycle/oxidative phosphorylation, respectively. This showed that glycolysis appeared globally down-regulated, with exception of *Pdk2*, *Pdk4*, and *Ldhb*, while TCA cycle and OXPHOS genes were globally up-regulated (Figure 4B and 4C). In line, detailed analysis of proteome data showed several proteins of the TCA cycle as well as the electron transport chain up-regulated in $Nf1^{Myf5}$ muscle (Figure 4D).

To directly measure mitochondrial oxidative metabolism, we employed high-resolution respirometry³¹ on freshly isolated muscle fibres from 5-week-old control and $Nf1^{Myf5}$ mice. We analysed the EDL muscle as a prototypical prevalently fast glycolytic muscle and the soleus muscle as a prototypical oxidative muscle for comparison (Figure 4E). First, non-phosphorylating leak respiration (= oxygen flux after addition fibres plus complex I substrates malate and pyruvate, with no ADP present) was unaffected in soleus and slightly although not significantly increased in EDL muscle of $Nf1^{Myf5}$ mice. Following the addition of ADP in saturating concentrations and glutamate, another complex I substrate, the

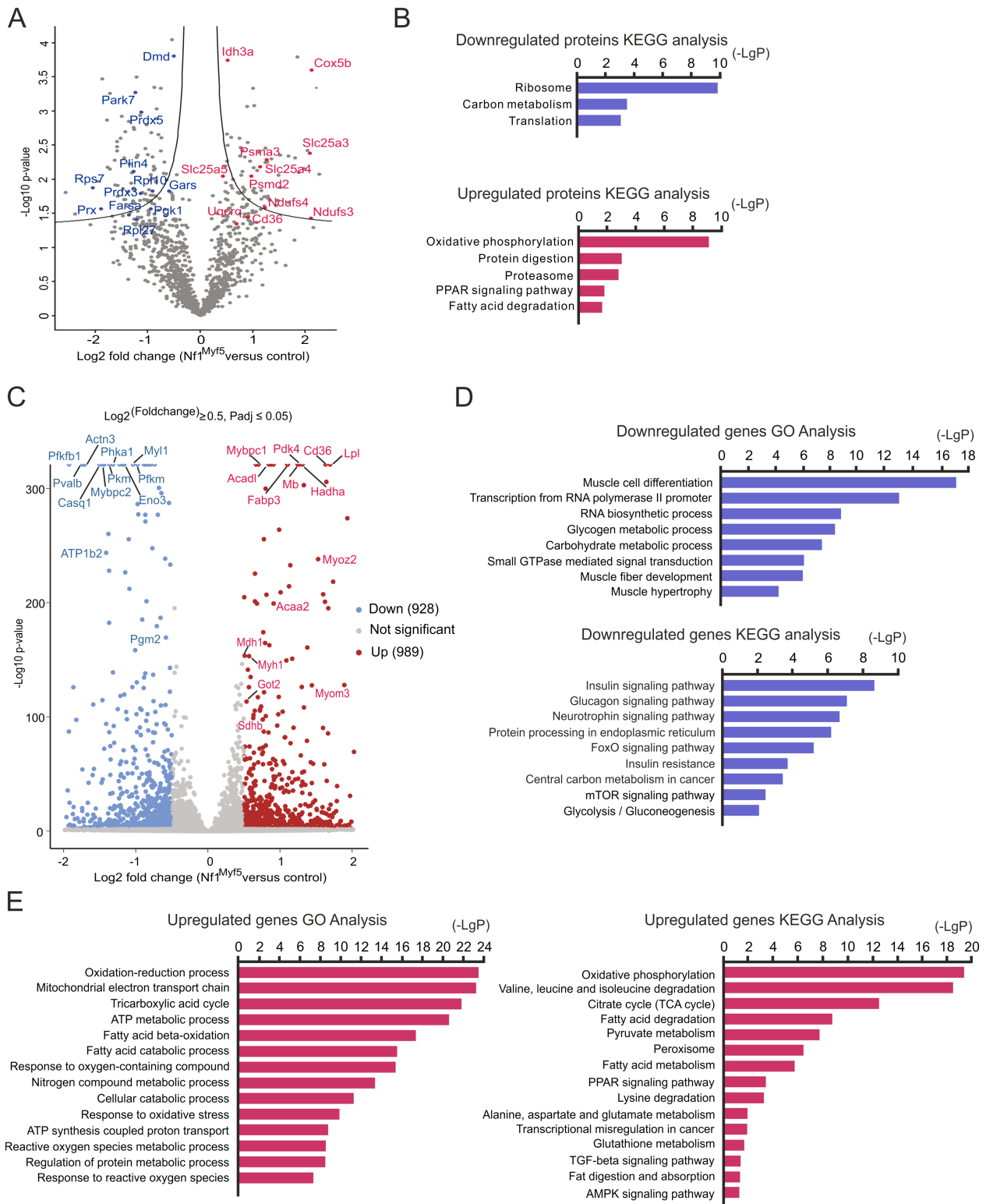


FIGURE 3 Proteome and transcriptome analyses of postnatal day 21 muscles. (A) Volcano plot of control vs. $Nf1^{Myf5}$ muscle proteome data. Individual deregulated proteins are indicated (blue: down-regulation, red: up-regulation). (B) KEGG pathway analysis of proteins down-regulated (top) and proteins up-regulated in $Nf1^{Myf5}$ muscle vs. control. (C) Volcano plot of control vs. $Nf1^{Myf5}$ muscle transcriptome data. Individual deregulated transcripts are indicated (blue: down-regulation, red: up-regulation). (D) Gene ontology (GO) and KEGG analysis of transcripts down-regulated in $Nf1^{Myf5}$ muscle vs. control. (E) GO and KEGG analysis of transcripts up-regulated in $Nf1^{Myf5}$ muscle vs. control.

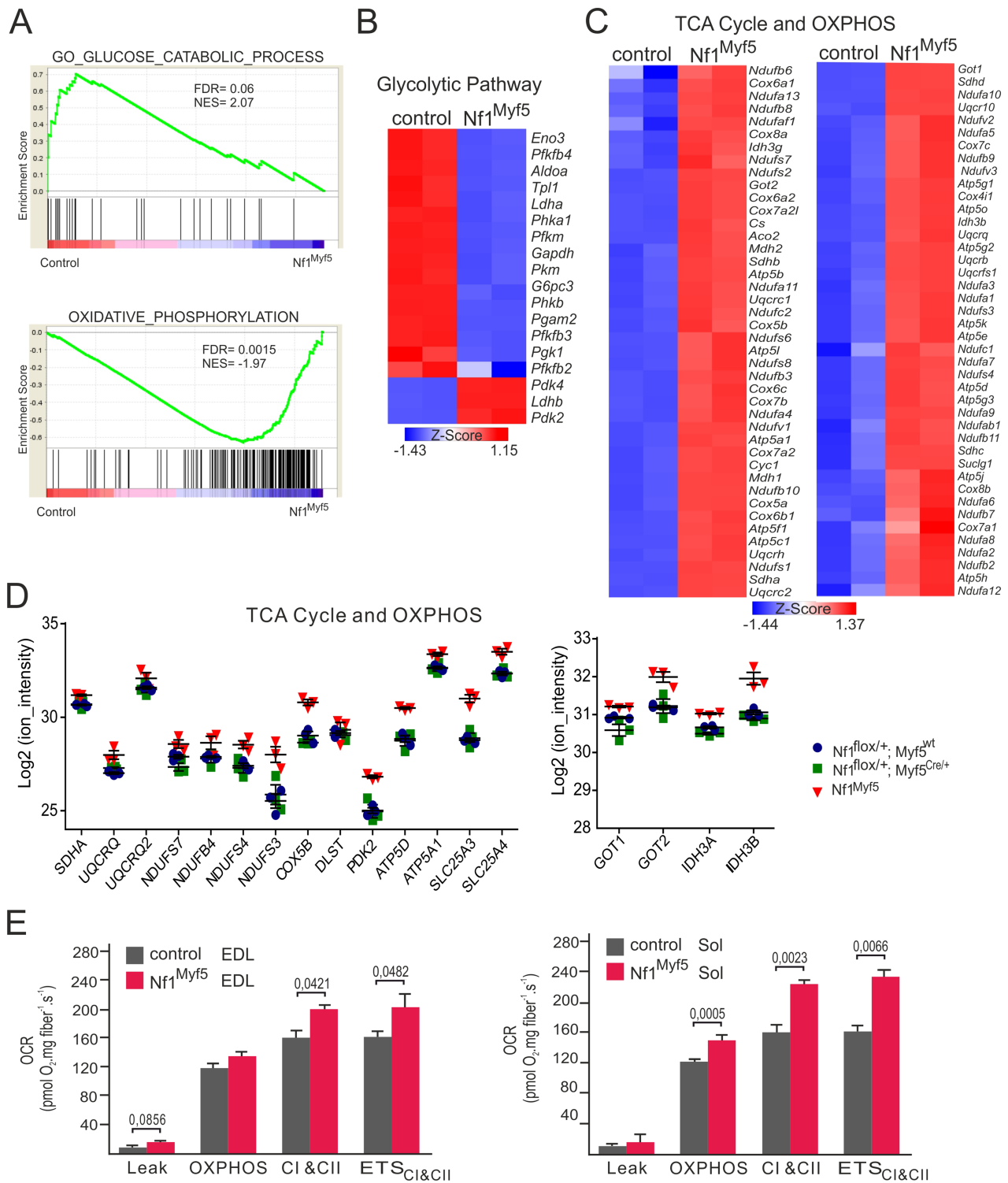


FIGURE 4 Disrupted metabolic homeostasis in $Nf1^{Myf5}$ muscle. (A) Gene set enrichment analysis (GSEA) of raw control vs. $Nf1^{Myf5}$ muscle transcriptome data for the terms ‘glucose catabolic process’ and ‘oxidative phosphorylation’. (B) Heat map of differentially expressed glycolytic genes (control vs. $Nf1^{Myf5}$ muscle). (C) Heat map of differentially expressed genes (control vs. $Nf1^{Myf5}$ muscle) of tricarboxic acid (TCA) cycle and oxidative phosphorylation machinery (OXPHOS) components. (D) Depiction of significantly deregulated proteins related to TCA cycle and OXPHOS. Proteome analysis of p21 muscle, genotypes are indicated. (E) Real-time high-resolution respirometry measurement of control vs. $Nf1^{Myf5}$ EDL (extensor digitorum longus) and Sol (soleus) muscles ($n = 7$ animals for both genotypes). Error bars represent standard error of means. P -value was calculated by two-sided unpaired t -test.

oxidative phosphorylation (OXPHOS) state, and subsequently the maximum coupled respiration through both mitochondrial complex I and II (CI&CII, after further addition of succinate) were measured, which were increased in both types of muscle of Nf1^{Myf5} mice, although the effects were more pronounced in soleus of Nf1^{Myf5} mice. Finally, maximum electron transfer system capacity (ETS_{CI&CII}, following addition of the exogenous mitochondrial uncoupler FCCP) confirmed the increased mitochondrial respiratory capacity in muscles of Nf1^{Myf5} animals (Figure 4E).

Glycolytic-to-oxidative fibre type shift in Nf1^{Myf5} muscle

Most muscles of the limbs consist of predominantly fast-twitching type 2 fibres, which are larger in diameter than slow-twitching type 1 fibres and produce main mechanical force. Type 2 fibres can be subdivided into type 2B fibres that show anaerobic glycolytic metabolism and type 2A fibres that use aerobic metabolism. Type 2B fibres express myosin heavy chain type 2B (MyHC-2B) or a combination of MyHC-2B and MyHC-2X (encoded by the *Myh4* and *Myh1* genes, respectively). Type 2A fibres express MyHC-2A encoded by *Myh2*, and type 1 fibres express MyHC-1 encoded by *Myh7*. Mining the p21 transcriptome data for markers of fast vs. slow fibres^{33,34} showed reduction of fast markers and increased expression of slow markers in Nf1^{Myf5} muscles (Figure 5A). Quantitative real-time PCR (RT-qPCR) confirmed up-regulation of *Myh2* and *Myh7* and down-regulation of *Myh4* mRNA in Nf1^{Myf5} muscle (Figure 5B). In accordance, protein levels of MyHC-1 were increased, and levels of MyHC-2B were decreased in Nf1^{Myf5} TA muscles (Figure 5C). This indicated distorted fast/slow fibre composition in Nf1^{Myf5} muscles.

The expression of fast fibre-related genes is induced in the first weeks of postnatal life in rodents.^{15,35} We therefore analysed the number of type 1 fibres in TA and EDL muscles (which are predominantly composed of fast fibres) over time (Figure 5D and 5E). At postnatal day 7 (p7), no differences were observed. But from postnatal day 14 (p14), a persistent slight increase in type 1 fibres in the TA muscle and a transient increase in the EDL muscle in Nf1^{Myf5} mice during postnatal development were seen (Figure 5D and 5E). We then analysed the proportion of type 2A and type 2B fibres in adult mice, revealing a shift of type 2B/X to type 2A fibres, that is, towards the fast oxidative phenotype, in Nf1^{Myf5} mice (Figure 5F and 5G). Of note, Nf1 was not differentially expressed in wild-type soleus (predominantly type 1 and 2A fibres) or TA (predominantly type 2b/X fibres) muscles (Figure 5H). We conclude that Nf1^{Myf5} muscles show a metabolic shift towards oxidative metabolism with partial conversion of type 2B/X to type 2A or type 1 fibres.

Defective protein homeostasis in Nf1-deficient muscles

Proteome analysis showed a significant down-regulation of several components of the translational machinery, especially ribosomal proteins as well as tRNA synthases (Figures 3A and 6A). Conversely, several proteasomal subunits were up-regulated (Figures 3A and 6B). This may indicate decreased protein synthesis and increased breakdown suggesting a mechanism paralleling myofibre atrophy. In line, RT-qPCR analysis demonstrated up-regulation of common atrophy-related transcripts^{36–38} in Nf1^{Myf5} muscle (Figure 6C). These genes comprise *Ctsl* (cathepsin L) and *Psm1* (proteasomal subunit alpha 1), or the classical atrogenes *Fbxo32* (atrogin-1/MAFbx) and *Trim63* (MuRF1).³⁹ Myofibre atrophy typically is caused by a dysbalance between protein synthesis and breakdown. Protein synthesis in skeletal muscle is mainly regulated via mTORC1.^{13,14} Interestingly, the KEGG term ‘mTOR signaling pathway’ was enriched in genes down-regulated in Nf1^{Myf5} muscle (Figure 3D). To analyse mTORC1 activity, we assessed phosphorylation of mTOR as well as the mTORC1 downstream target S6 ribosomal protein. p21 Nf1^{Myf5} muscle tissue showed hallmarks of decreased mTORC1 signalling, with decreased phosphorylation of mTOR Ser2448 and decreased S6 Ser235/236 phosphorylation (Figure 6D). Altogether, this suggests disturbed protein homeostasis in Nf1^{Myf5} muscle with decreased mTORC1-driven protein synthesis and increased protein breakdown. Such alterations may be the result of a muscular energy deficit.¹³ In line, Nf1^{Myf5} muscle showed increased levels of phosphorylated AMP-dependent kinase (AMPK), the most prominent intracellular energy sensor (Figure 6E). In sum, Nf1^{Myf5} animals show typical signs of muscle atrophy with decreased anabolic signalling, in combination with an unmet energy demand.

Increased fatty acid catabolism in Nf1^{Myf5} muscle

Increased oxidative metabolism, but concomitant down-regulation of glycolytic genes, indicated that Nf1^{Myf5} muscles may predominantly use fatty acids to feed the TCA cycle. Analysis of proteome as well as transcriptome data highlighted terms associated with fatty acid catabolism, as ‘fatty acid degradation’ (proteome) or ‘fatty acid beta-oxidation’ (transcriptome) were significantly enriched amongst proteins/mRNAs up-regulated in Nf1^{Myf5} muscle (Figure 3B and 3E). Accordingly, several proteins associated with cellular lipid uptake and breakdown were up-regulated in Nf1^{Myf5} muscle (Figure 7A). In line with GO and KEGG analysis of differentially expressed genes, GSEA of transcriptome data showed genes belonging to the clusters ‘fatty acid beta-oxidation’ and ‘fatty acid catabolic process’ strongly enriched in Nf1^{Myf5} muscle (Figure 7B). Indeed,

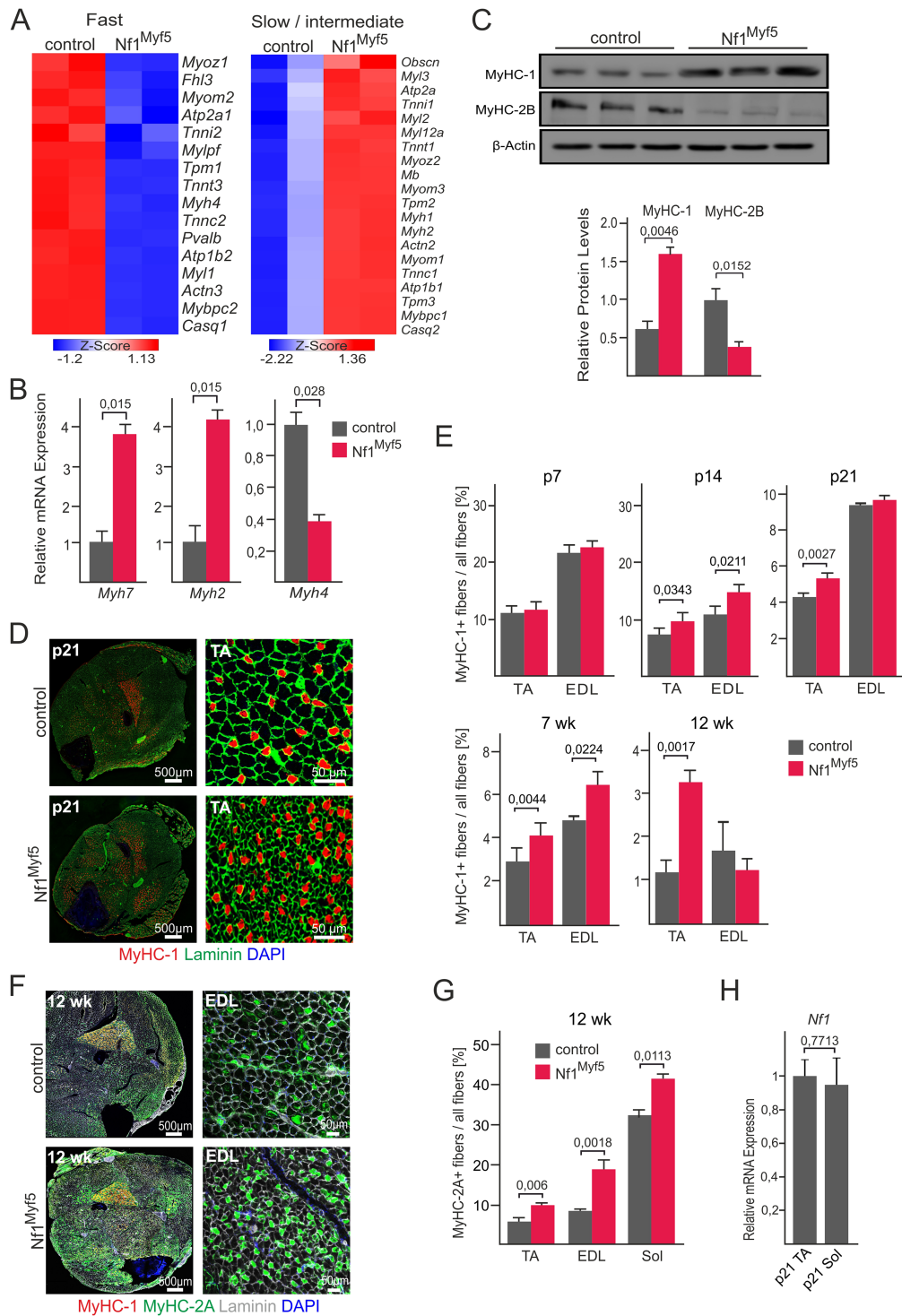


FIGURE 5 Fibre type shift in *Nf1^{Myf5}* muscle. (A) Heat maps showing differentially expressed genes specific for fast or slow/intermediate fibres, respectively, between control and *Nf1^{Myf5}* muscle. (B) RT-qPCR analysis of myosin heavy chain genes *Myh7*, *Myh2*, and *Myh4* on control vs. *Nf1^{Myf5}* muscle ($n = 3$ animals per genotype). (C) Western blot analysis of myosin heavy chain type 1 (MyHC-1) and type 2B (MyHC-2B) on control vs. *Nf1^{Myf5}* muscle. Quantification below ($n = 3$ animals per genotype). (D) Immunolabelling for MyHC-1 on cross sections of p21 control vs. *Nf1^{Myf5}* lower legs. TA muscles are shown as magnifications right. Sections are stained for laminin and DAPI. (E) Quantification of type 1 fibres/all fibres for indicated postnatal time points on TA and EDL muscles ($n = 3$ animals per genotype). (F) Immunolabelling for fast oxidative fibre type myosin (MyHC-2A) and MyHC-1 on cross sections of control vs. *Nf1^{Myf5}* lower legs. Sections are stained for laminin and DAPI. EDL muscles are shown as magnifications right. (G) Quantification of percentage of MyHC-2A fibres/all fibres ($n = 3$ animals per genotype). (H) RT-qPCR analysis of *Nf1* expression between wild-type p21 TA and Sol muscles. Error bars represent standard error of means. *P*-value was calculated by two-sided unpaired *t*-test.

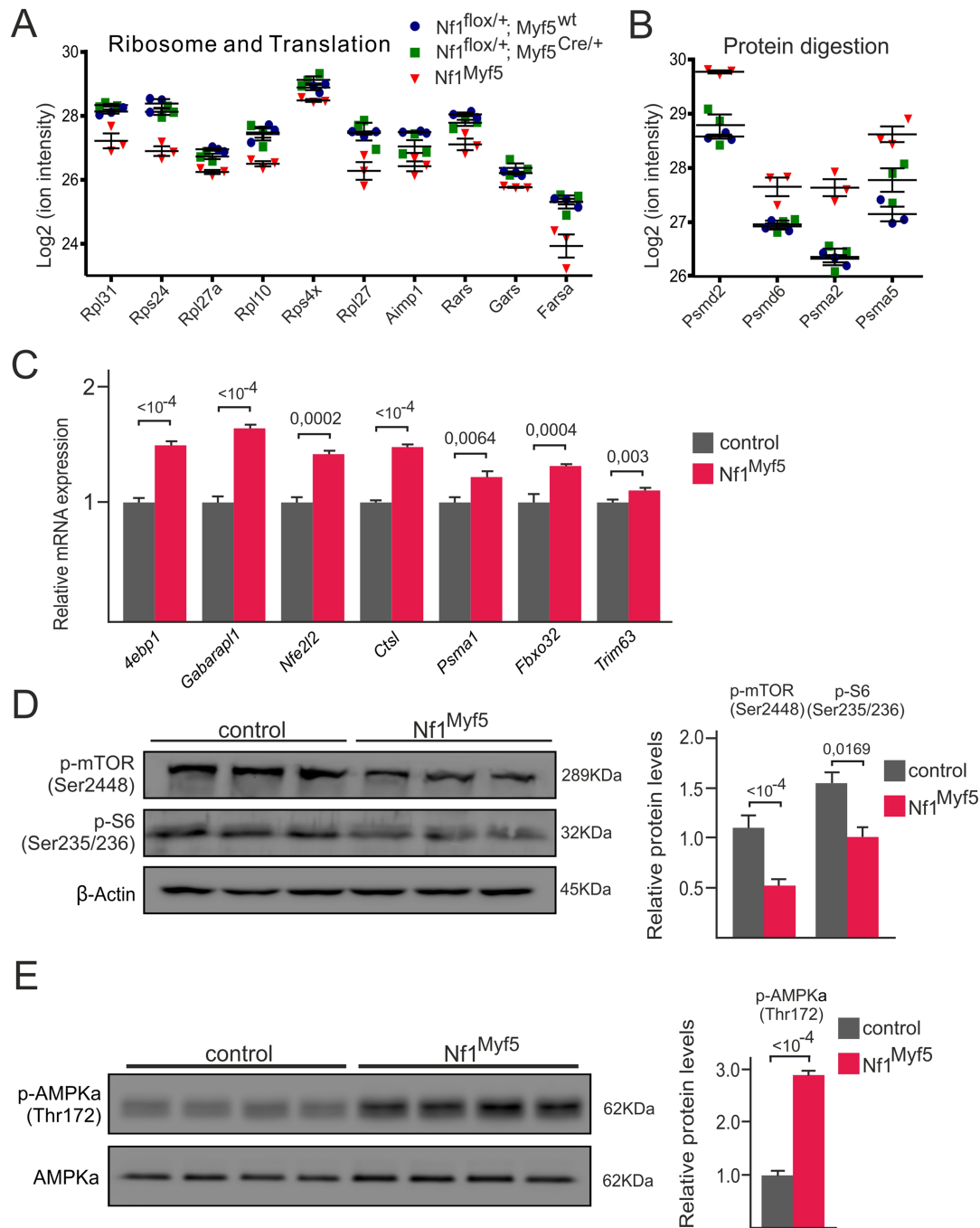


FIGURE 6 Disturbed protein homeostasis and energy deficit in Nf1^{Myf5} muscle. (A) Depiction of significantly deregulated components of the ribosome and proteins related to translation. Proteome analysis of p21 muscle, genotypes are indicated. (B) Depiction of significantly deregulated proteins related to the KEGG term 'protein digestion'. Proteome analysis of p21 muscle, genotypes are indicated. (C) RT-qPCR analysis of p21 control and Nf1^{Myf5} muscle for transcripts related to muscle atrophy ($n = 3$ animals per genotype). (D) Western blot analysis for phosphorylated mTOR (Ser2448) and phosphorylated S6 ribosomal protein (Ser235/236). Quantification shown right ($n = 3$ animals per genotype). (E) Western blot analysis for phosphorylated AMPK (Thr172). Quantification shown right ($n = 4$ animals per genotype). Error bars represent standard error of means. P -value was calculated by two-sided unpaired t -test.

numerous genes belonging to the GO term 'fatty acid metabolism' were up-regulated in Nf1^{Myf5} muscle (Figure 7C), including the gene encoding the main fatty acid transporter Cd36, or several acyl-CoA dehydrogenases, which not only

play a role in β -oxidation but also breakdown of branched amino acids. Up-regulation of several genes of this panel in Nf1^{Myf5} muscle (*Lpl* encoding part of the enzyme complex responsible for lipid uptake, fatty acid binding proteins

Fabp3 and *Fabp4*, carnitine palmitoyltransferases *Cpt1b* and *Cpt2*, and *Acad1* encoding medium chain acyl-CoA dehydrogenase) was confirmed by RT-qPCR (Figure 7D). In sum, proteome as well as transcriptome data indicate increased fatty acid breakdown in *Nf1^{Myf5}* muscle to fuel the TCA cycle and OXPHOS. As opposed to *Nf1^{Prx1}* mice, we did not observe increased muscle interstitial adipose tissue (Figure 7E). Contrasting previous reports,²² we did not find indication of ectopic lipid storage in muscle fibres in our muscle-specific *Nf1* mutants at 1 or 12 weeks of

age (Figure 7E; Supporting Information, Figure S5A and S5B).

PPAR γ has been involved in promoting intramuscular lipolysis.^{40,41} In muscle tissue of *Nf1^{Myf5}* mice, we found over-expression of *Pparg* mRNA (Figure 7F); specific up-regulation of PPAR γ isoform 1 was confirmed on the protein level in 7-week-old and also already in 2-week-old animals (Figure 7G). In line, GSEA showed enrichment for ‘adipogenic targets of PPAR γ ’ enriched in *Nf1* mutants (Figure 7H). Similarly, ‘PPAR signaling pathway’ was enriched in transcripts and

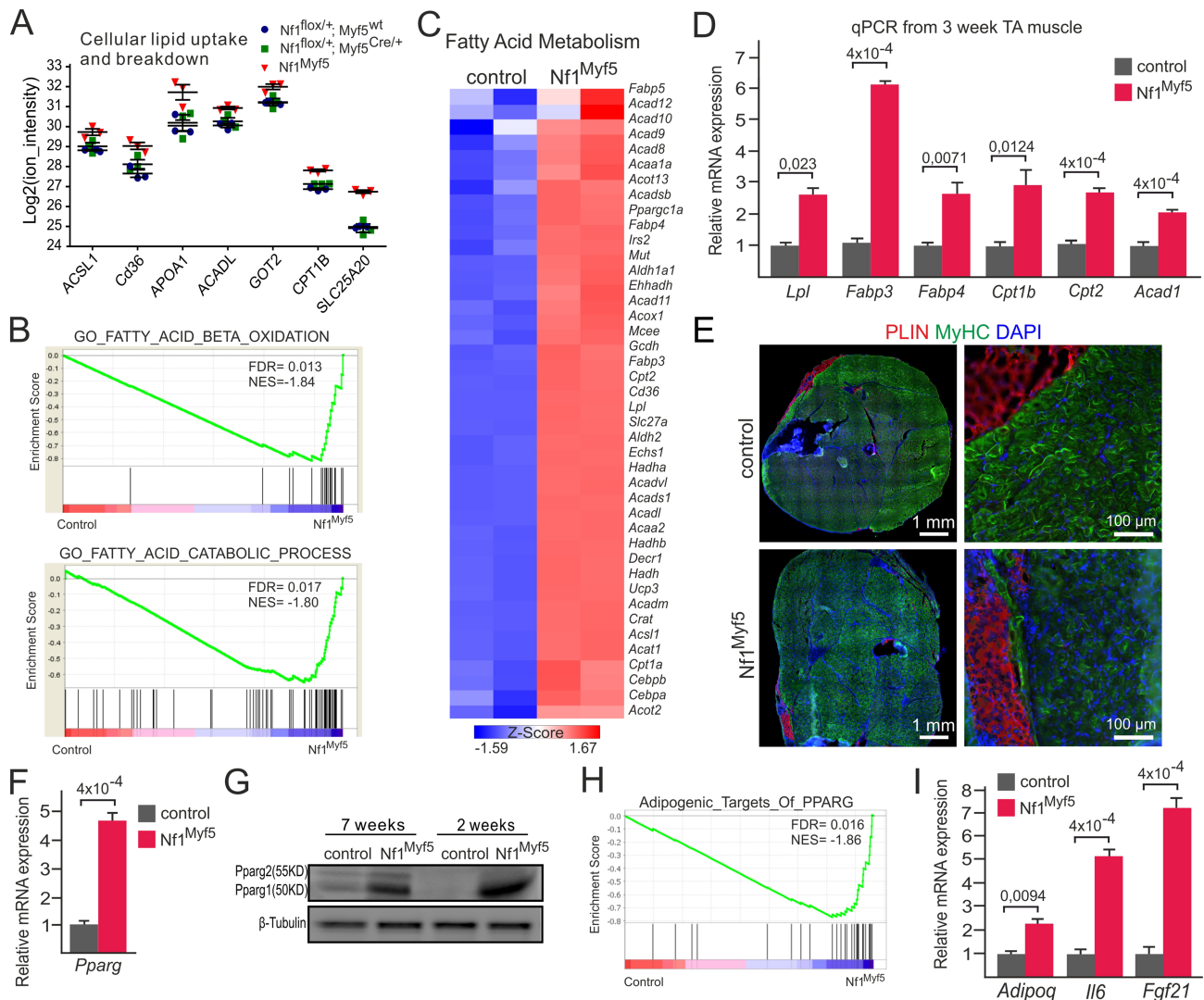


FIGURE 7 Increased fatty acid oxidation in *Nf1^{Myf5}* muscle. (A) Depiction of significantly deregulated proteins related to cellular lipid uptake and breakdown. Proteome analysis of p21 muscle, genotypes are indicated. (B) Gene set enrichment analysis (GSEA) of control vs. *Nf1^{Myf5}* muscle transcriptome data for the terms ‘fatty acid beta-oxidation’ and ‘fatty acid catabolic process’. (C) Heat map of differentially expressed genes related to fatty acid metabolism (control vs. *Nf1^{Myf5}* muscle). (D) RT-qPCR analysis in control vs. *Nf1^{Myf5}* muscle of selected genes related to fatty acid uptake, transport, and catabolism ($n = 3$ animals per genotype). (E) Perilipin (PLIN, red) and MyHC (green) immunolabelling on 12-week-old control vs. *Nf1^{Myf5}* muscle. Overview tile scan images left, magnifications showing subcutaneous adipose tissue and adjacent muscle tissue shown right. (F) RT-qPCR analysis of *Pparg* in control vs. *Nf1^{Myf5}* muscle ($n = 3$ animals per genotype). (G) Western blot analysis for PPAR γ on control vs. *Nf1^{Myf5}* muscle. (H) GSEA of control vs. *Nf1^{Myf5}* muscle transcriptome data for the term ‘adipogenic targets of PPAR γ ’. (I) RT-qPCR analysis for *Adipoq*, *Il6*, and *Fgf21* on control vs. *Nf1^{Myf5}* muscle ($n = 3$ animals per genotype). Error bars represent standard error of means. P -value was calculated by two-sided unpaired t -test.

proteins up-regulated in Nf1 mutants (Figure 3B and 3E). PPAR γ was shown to induce the myokine adiponectin (Adipoq).⁴² Nf1-deficient muscle showed increased expression of *Adipoq* as well as mRNAs of the myokine *Il6* and the catabolic cytokine *Fgf21* (Figure 7I).

Paucity of white adipose tissue in Nf1^{Myf5} mice

Finally, increased fatty acid consumption in Nf1^{Myf5} muscles as indicated by proteome and transcriptome analyses suggests increased lipid mobilization from adipose tissue. Indeed, Nf1^{Myf5} animals showed a drastic reduction of their white

adipose tissue (WAT), affecting both subcutaneous and visceral WATs (Figure 8A and 8B). This was specific to WAT; brown adipose tissue (BAT) depots were unaffected (Figure 8B). In histology, WAT appeared denser, deprived of lipid content (Figure 8C). In line, RT-qPCR analysis showed mild induction of *Lipe* encoding hormone-sensitive lipase (Figure 8D), and strong induction of *Pnpla2* encoding adipose triglyceride lipase (ATGL), the rate-limiting enzyme of lipolysis (Figure 8D). *Dgat2* encoding diacylglycerol O-acyltransferase 2, the rate-limiting enzyme of lipogenesis, was not significantly induced (Figure 8D). Decreased expression of *Lpl* and *Cd36* in WAT of Nf1^{Myf5} mice (Figure 8D; Supporting Information, Figure S6A) suggests decreased lipid uptake, and decreased

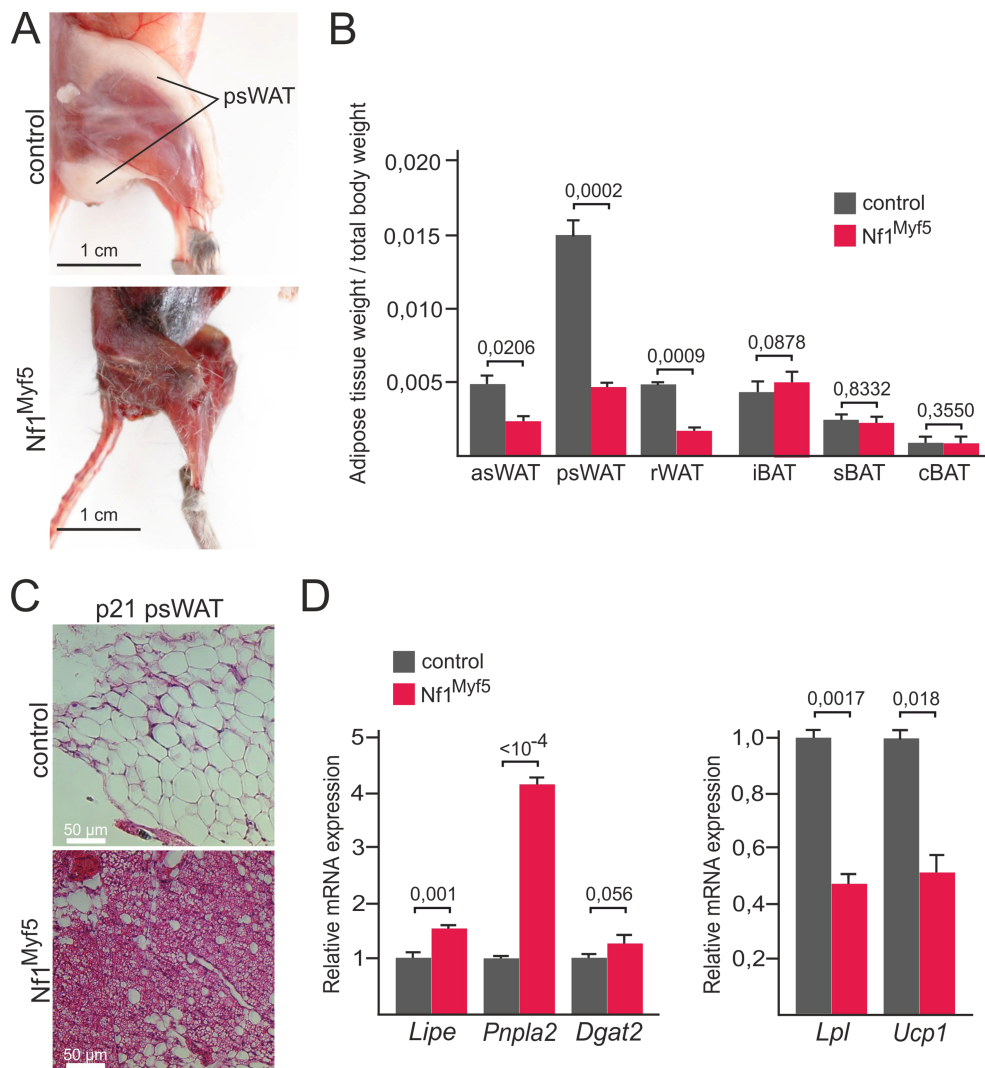


FIGURE 8 Paucity of white adipose tissue in Nf1^{Myf5} mice. (A) Nf1^{Myf5} (p21) mice show reduced posterior subcutaneous white adipose tissue (WAT). Note dark red appearance of muscles in Nf1^{Myf5} mutant. (B) Weight of adipose tissue depots of control vs. Nf1^{Myf5} mice at 12 weeks of age. Adipose depot weight was normalized to body weight. AsWAT, anterior subcutaneous white adipose tissue; psWAT, posterior subcutaneous white adipose tissue; rWAT, retroperitoneal white adipose tissue; iBAT, interscapular brown adipose tissue; sBAT, subscapular brown adipose tissue; cBAT, cervical brown adipose tissue ($n = 4$ animals per genotype). (C) Histological analysis (haematoxylin and eosin) of p21 psWAT of control vs. Nf1^{Myf5} mice. (D) RT-qPCR analysis of p21 psWAT of control vs. Nf1^{Myf5} mice for *Lipe*, *Pnpla2*, *Dgat2*, *Lpl*, and *Ucp1* ($n = 3$ animals per genotype). Error bars represent standard error of means. P -value was calculated by two-sided unpaired t -test.

expression of *Plin1* confirms decreased lipid storage (Supporting Information, Figure S6A). *Ucp1* was not induced but rather down-regulated in Nf1^{Myf5} WAT (Figure 8D), suggesting no 'browning' of WAT. Expression of *Pparg* was unaltered in Nf1^{Myf5} posterior subcutaneous WAT, as were *mtCo1* and *Cs* (encoding mitochondrial cytochrome c oxidase and citrate synthase, respectively) as representatives of electron transport chain and TCA cycle (Supporting Information, Figure S6A). BAT originates in large part from a dermomyotomal Myf5⁺ progenitor population⁴³; thus, Nf1 inactivation in BAT may influence the phenotype. Intriguingly, RT-qPCR analysis of BAT showed some overlap in gene deregulation with Nf1-deficient muscle, as *mtCo1* was up-regulated; however, *Cs*, *Pparg*, and also *Ucp1* were unaltered (Supporting Information, Figure S6B) suggesting no major influence on BAT. This altogether suggests a general catabolic state of Nf1^{Myf5} animals forced by unmet energetic need of muscle tissue leading to a cachectic state with increased lipid mobilization.

Discussion

We show here that Nf1 inactivation specifically in the myogenic lineage leads to postnatal myopathy mirroring a key feature seen in Nf1 patients. Thus, the Nf1^{Myf5} line enables analysis of Nf1 function in postnatal muscles and in comparison with models as the Nf1^{Prx1} mouse is suitable to distinguish muscle specific from non-myogenic functions of Nf1. Nf1^{Myf5} mice are viable, while Nf1^{Lbx1} (this study) and Nf1^{MyoD} mice²² were postnatally lethal. This difference may be caused by different efficacy of the Cre driver lines used. *Lbx1*^{Cre} efficiently targets early migrating myogenic progenitors, including those of the diaphragm and tongue,²⁴ and expression of *Lbx1* precedes the expression of *Myf5*.⁴⁴ While *MyoD* is expressed in all myogenic cells, not all myoblasts have experienced expression of *Myf5*, although there is dispute whether *Myf5* and *MyoD* cells represent partially separate lineages.^{45–48} Thus, very likely not all myogenic cells are targeted in the Nf1^{Myf5} model, possibly alleviating the phenotype to a life-compatible level. Depletion of the *Myf5* lineage led to compensatory takeover by *MyoD*-lineage cells,⁴⁵ and Comai *et al.*⁴⁶ demonstrated a marked compensatory effect of recombination escapers upon *Myf5* cell depletion. Importantly, robust knockdown of *Nf1* mRNA in Nf1^{Myf5} mice at p21 argues against a possible lineage takeover of *Myf5*-negative cells or of recombination escapers, suggesting that no significant skewing of the myogenic lineage had occurred in our model.

Nf1^{Myf5} mice did not show increased interstitial fibrotic and adipogenic infiltration of muscle as it was seen after inactivation of Nf1 in limb mesenchyme via *Prx1*^{Cre}.¹⁹ Muscle interstitial fibroblasts and adipocytes do not originate from myogenic cells but from non-myogenic mesenchymal

progenitors, the so-called fibro-adipogenic progenitors.^{49–51} These cells in turn derive from lateral plate mesoderm-derived limb bud mesenchyme.⁵² The same developmental mesenchymal progenitors also form muscle interstitial fibroblasts and adipocytes during development.⁵³ *Prx1*^{Cre} targets the entire limb mesenchyme²¹ encompassing this mesenchymal progenitor population during development.⁵⁴ Thus, comparing Nf1^{Prx1} and Nf1^{Myf5} models, we conclude that fibro-fatty infiltration of muscle in the Nf1-*Prx1* model does not originate from myogenic cells but from interstitial mesenchymal cells. However, in another model of muscle-specific inactivation of Nf1 (*MyoD*^{Cre}), ectopic intramyocellular lipid accumulation was reported,²² which we did not observe in our model. This discrepancy might be caused by the different Cre drivers used; of note, *MyoD*^{Cre} was reported to be active in the developing liver⁵⁵; thus, an indirect effect may not be excluded.

Nf1^{Myf5} mice show reduced postnatal fibre growth that manifested early in life. This suggests that loss of Nf1 does not induce muscle atrophy at a specific time point but rather that NF1-associated muscle weakness is a continuous process of decreased hypertrophic growth beginning in childhood. Indeed, muscle weakness and decreased muscle cross-sectional area are already seen in paediatric patients.^{7,8} This strongly suggests that muscular manifestations in NF1 are predominantly a developmental disorder and any treatment towards an amelioration of the muscular phenotype would have to encompass this critical phase. In line with this, a recent study showed that treatment of *Prx1*^{Cre};Nf1^{flox/flox} mice with the MEK inhibitor PD0325901 starting at 4 weeks after birth did not result in appreciable amelioration of the muscular phenotype.⁵⁶ In Nf1^{Myf5} mice, predominantly fast (type 2) fibres are affected. In general, type 2 fibres have higher potential for hypertrophy than type 1 fibres, which also makes them more vulnerable for atrophy.⁵⁷ Nevertheless, different myopathies predominantly affect different fibre types; the underlying cause is mostly unclear.¹⁶ Our results indicate dysbalanced protein homeostasis in Nf1^{Myf5} muscle. TORC1 signalling is a master regulator for protein synthesis.^{13,14} Nf1^{Myf5} muscle showed reduced mTORC1 activation that is in line with proteome and transcriptome data, altogether indicating decreased capacity for protein synthesis. This may also contribute to the divergence of our proteome and transcriptome datasets. On the other hand, common atrogenes were up-regulated on the transcript level, and proteasomal components were up-regulated on transcript and protein levels, in addition suggesting increased protein breakdown. Thus, Nf1-associated muscle atrophy appears to overlap general mechanisms observed in other atrophy conditions including myopathies, sarcopenia, and cachexia, that is, excessive protein breakdown and decreased protein synthesis.¹³

In parallel, we observed a fibre type shift from glycolytic type 2 fibres to oxidative type 2 and in part to type 1 fibres. In adult Nf1^{Prx1} mice, no fibre type shift was reported²⁰; however, this had not been quantified. During embryonic and

foetal myogenesis, muscle fibres predominantly show oxidative type gene and protein expression. Fast-type gene and protein expression is first detected during late foetal development; the major slow-to-fast fibre type change occurs during the early postnatal period.¹⁵ The emergence of different fibre types in development is under control of transcription factors such as *Six1*, *Six4*, *Sox6*, *Tbx15*, *Prdm1* (aka *Blimp1*), and *Nfix*^{58–64}; however, we did not detect a significant deregulation of these factors in our transcriptome data (Supporting Information, *Data S1*). Mature fibres have a degree of plasticity and can shift their metabolism based on, for example, endurance vs. peak force training.¹⁵ Importantly, fibre type shifts are involved in muscular disorders and muscle aging.^{15,16} Nf1 is best known as a Ras-GTPase-activating protein that negatively regulates downstream MEK–ERK signalling.¹ Interestingly, ERK1/2 activity itself was involved in regulating muscle fibre types previously.¹⁵ In line, it was recently shown that expression of an activated form of MEK1 in muscle fibres can drive a metabolic shift to oxidative fibres.⁶⁵

In line with increased oxidative metabolism relying on fatty acid consumption, Nf1^{Myf5} mice showed severe reduction of WAT. Strong induction of lipolytic enzymes (HSL and ATGL), but no significant induction of lipogenic enzyme DGAT2, suggests an overweight of lipolysis over lipogenesis. In line, reduced Plin1 levels were associated with increased lipolysis.⁶⁶ Increased lipid mobilization leading to loss of adipose tissue is a hallmark of cancer cachexia. As in our model, this is frequently attributed to increased lipolysis associated with up-regulation of ATGL expression.⁶⁶ Myf5^{Cre}-mediated gene inactivation preferentially targets the myogenic lineage; however, it also targets BAT as well as several (anteriorly located) WAT depots.⁶⁷ Thus, inactivation of *Nf1* in subsets of adipocyte progenitors may have a direct effect on adipogenesis/adipocyte function. Inactivation of the tumour suppressor *Pten*, leading to hyperactivation of the PI3K pathway, in the Myf5 lineage led to increased size of anterior BAT and WAT depots, while posterior WAT depots were virtually absent in mutants.⁶⁸ We did not detect differences in BAT size in Nf1^{Myf5} mice. Moreover, *Ucp1* mRNA was not up-regulated in BAT, indicating that Nf1-deficient BAT does not show increased energy expenditure. WAT depots were reduced irrespective of anatomical location; anterior subcutaneous WAT and retroperitoneal WAT that are targeted by Myf5^{Cre}, as well as posterior subcutaneous WAT that is not targeted,⁶⁷ were strongly affected. This argues against a cell autonomous effect on *Nf1* deletion in adipogenic progenitors/adipocytes, but rather in favour of a muscle-derived effect enforcing lipolysis in WAT.

We observed up-regulation of mRNAs encoding myokines, that is, muscle-produced endocrine signalling factors. FGF21 and IL6 were shown to stimulate lipolysis in WAT.^{69,70} IL6 also stimulates lipolysis and fatty acid oxidation in muscle in an autocrine fashion, interestingly via AMPK activation.^{71–73} Furthermore, *Adipoq*, encoding adiponectin, was induced.

Adiponectin is mainly known as an adipokine; however, also skeletal muscle produces adiponectin, and *Adipoq* knockout mice show increased intramyocellular lipid content.⁷⁴ Adiponectin expression in muscle can be induced by PPAR γ ,⁴² which was overexpressed in Nf1^{Myf5} muscle. PPAR γ in muscle promotes fatty acid oxidation.^{40,41} PPAR γ overexpression in muscle protects from obesity-induced diabetes, leads to increased adiponectin expression, and induces oxidative metabolism, and muscles have reduced lipid content.⁴² Conversely, muscle-specific inactivation of PPAR γ induces obesity and insulin resistance.^{75,76} FGF21 is well described as mitochondrial stress-induced myokine.^{77–79} Very recently, FGF21 was described as a novel player in the regulation of muscle mass during fasting-induced muscle atrophy and weakness.⁸⁰ Here, we describe a strong induction of muscle *Fgf21* in response to genetic ablation of *Nf1*, together with a dramatic reduction of WAT depots, affecting both subcutaneous and visceral WATs. However, future studies are warranted to clarify the protective or detrimental catabolic action of FGF21 via inter-tissue crosstalk in Nf1^{Myf5} animals.

Contrasting increased oxidative metabolism and fatty acid breakdown, down-regulation of all glycolysis components in the transcriptome analysis indicated decreased glycolytic flux in Nf1^{Myf5} muscles. Intriguingly, *Pdk2*, *Pdk4*, and *Ldhb* were up-regulated. The B-isoform of LDH is mainly expressed in oxidative muscle, and overexpression of *Ldhb* increases oxidative metabolism⁸¹ in line with the oxidative phenotype we observe. PDK2 and PDK4 negatively regulate pyruvate dehydrogenase and thus impair funneling pyruvate from glycolysis towards usage in the TCA cycle, shunting mitochondrial metabolism towards fatty acid usage.¹⁵ This altogether suggests that utilization of glucose as fuel for the TCA cycle is impaired in Nf1^{Myf5} muscle; thus, fatty acids as alternative energy source need to be used. Intriguingly, a decreased respiratory quotient indicating lower carbohydrate and increased lipid oxidation was demonstrated in NF1 patients.⁸² Thus, defective glycolysis may therefore explain why Nf1^{Myf5} muscles shift towards oxidative metabolism and primarily rely on fatty acids but could also contribute to the apparent energy deficit of Nf1-deficient muscle indicated by AMPK activation. Nf1 is well known as a tumour suppressor gene repressing RAS signalling. Increased RAS signalling or loss of Nf1 is typically associated with the induction of a Warburg effect, that is, increased glycolytic flux under aerobic conditions, as well as the induction of pathways supporting cell growth, as mTORC1.^{83,84} Why loss of Nf1 in myogenic cells leads to effectively opposite outcome is unknown; however, it indicates differences in either the cellular environment or intracellular signal reception that lead to a different interpretation of Nf1-dependent signals. Decreased energy charge is sensed in cells via AMPK that is a master regulator of cellular energy homeostasis.⁸⁵ Activation of AMPK can reduce mTORC1 activity and thus protein synthesis, providing a possible explanation for the reduced hypertrophic growth of

Nf1^{Myf5} muscles. In turn, AMPK activation is known to induce mitochondrial biogenesis, glucose uptake, and fatty acid consumption.^{85,86} This altogether suggests that impaired glycolysis may be the primary defect in Nf1^{Myf5} muscle, leading to an energy deficit, shifting cellular metabolism via AMPK towards OXPHOS.

Mitochondria are described as the predominant source of reactive oxidant species (ROS) in muscle fibres.⁸⁷ Notably, oxidative stress in skeletal muscles can promote protein synthesis/degradation imbalance and muscle wasting.⁸⁸ Increased ROS levels in cachectic muscle could be attributed to the reduction in the activity of endogenous antioxidant enzymes.⁸⁹ In drosophila, loss of Nf1 caused mitochondrial oxidative stress concomitant to decreased ATP production.⁹⁰ GO and KEGG analysis of transcriptome data showed enrichment of the terms 'response to oxygen-containing compound', 'response to oxidative stress', 'reactive oxygen species metabolic process', 'response to reactive oxygen species (GO)', and 'glutathione metabolism' (KEGG) in genes up-regulated in Nf1^{Myf5} muscle (Figure 3E). In addition, transcriptome analysis showed increased expression of NADPH oxidase genes *Cybb* (*Nox2*) and *Nox4* (Supporting Information, Data S1), which are an additional source of ROS.⁹¹ This indicates that increased mitochondrial respiration in Nf1^{Myf5} muscle may lead to oxidative stress, hampering mitochondrial energy production. This raises the question whether a concomitant increased mitochondrial ROS production may even aggravate the situation in Nf1^{Myf5} mice, potentially causing a vicious cycle.

In summary, Nf1^{Myf5} represents a viable mouse model for muscle-specific inactivation of Nf1 that recapitulates the paediatric myopathy seen in NF1 patients. Nf1 deficiency disrupts metabolic homeostasis in muscle leading to muscular energy deficit and a catabolic state causing reduced postnatal muscle hypertrophy. As postnatal muscle growth is carried by a combination of cell accrual and protein synthesis,^{11,12} Nf1 deficiency may also alter behaviour of Myf5⁺ myogenic progenitors, which should be addressed in future studies.

Author contributions

X.W. and S.S. developed the study concept and design. X.W. performed the majority of experiments and data collection. J.F., M.O., K.W., A.C.P., S.B., B.T., D.M., A.K., and S.K. performed additional experiments or provided resources. X.W., M.O., D.M., A.K., and S.S. interpreted data. X.W. and S.S. prepared the figures. M.O., A.K., S.K., and S.S. wrote the manuscript. All authors declare that the submitted work has not been published before (neither in English nor in any other language) and that the work is not under consideration for publication elsewhere. The authors of this manuscript certify that they comply with the ethical guidelines for authorship

and publishing in the *Journal of Cachexia, Sarcopenia and Muscle*.⁹²

Acknowledgements

We thank the animal facility of the Max Planck Institute for Molecular Genetics, Berlin, for expert support, especially Katja Zill and Ludger Hartmann. X.W. was supported by the Chinese Scholarship Council (CSC) and the Sonnenfeld Stiftung Berlin. K.W. and A.K. were supported by a grant from the German Ministry of Education and Research (BMBF) and the State of Brandenburg (DZD grant 82DZD00302).

Online supplementary material

Additional supporting information may be found online in the Supporting Information section at the end of the article.

Figure S1 Characterization of Lbx1Cre and Myf5Cre specificity (A, B) Analysis of Lbx1Cre and Myf5Cre specificity. Cre mice were bred to Rosa26mTmG reporter mice and analyzed at embryonic day 18 (E18.5; A) or postnatal day 21 (p21; B). Staining: green depicts mG reporter activity tracing recombined cells, red depicts mT reporter activity tracing non-recombined cells. Satellite cells have been stained for Pax7, neurons for β -tubulin III (purple). TB: Triceps brachii; CT: connective tissue; EDL: Extensor digitorum longus; TA: Tibialis anterior.

Figure S2 Extended data for pre- and postnatal characterization of Nf1Myf5 animals (A) Whole-mount in-situ hybridization of 14 day old control and Nf1Myf5 embryos for Myod. Quantification of Myod+ area in limbs is shown right (n=3 animals per genotype). (B) RT-qPCR analysis of Nf1 expression in p21 Tibialis anterior (TA) muscles of Nf1+/+, Myf5Cre;Nf1flox/+ and Myf5Cre;Nf1flox/flox animals (n=3 animals per genotype). (C) RT-qPCR analysis of Myf5 expression from Myf5+/+, Nf1flox/+ vs. Myf5Cre/+;Nf1flox/flox animals in E18.5 limb muscles and p21 TA muscle (n=3 animals per genotype). (D) Quantification of total myofiber numbers in muscles (TB: Triceps brachii, TA: Tibialis anterior, EDL: Extensor digitorum longus) of p21 control and Nf1Myf5 animals (n=3 animals per genotype). Error bars represent standard error of means (SEM). P-value was calculated by two-sided unpaired t-test. P-value above 0,05 was considered not significant (N.S.).

Figure S3 Extended data proteome and transcriptome analysis (A, B) Principal component analysis (PCA) of proteome (A) and transcriptome (B) data. Genotypes are indicated. (C) Correlation analysis of transcriptome and proteome data. The Pearson correlation coefficient between transcript and

protein levels of Nf1Myf5 and control TA muscles are shown as a log₂-fold change (all squares, -0.144). Specific factors involved in the ETC (red, -0.0796) and the TCA cycle (green, -0.595) are highlighted. Pathway identities were retrieved from KEGG.

Figure S4 Blood glucose and insulin signaling in Nf1Myf5 mice (A) Blood glucose test in 5 weeks old Nf1Myf5 animals (n=7 animals per genotype; each dot represents measurement from one individual animal). (B) Western blot analysis for phosphorylated AKT (Ser473) and phosphorylated IRS1 (Ser1101, Ser 636/639). (C) Quantification of p-AKT(s473), p-IRS1(s1101) and p-IRS1(s636/639) relative to β -actin levels (top); bottom: β -actin was equally abundant in control and Nf1Myf5 samples, measured relative to Ponceau S staining (n=3 animals per genotype). Error bars represent standard error of means (SEM). P-value was calculated by two-sided unpaired t-test.

Figure S5 Extended data for lipid metabolism in Nf1Myf5 muscle (A) Hind limb cross sections of 1 week (top) and 12 week (bottom) control and Nf1Myf5 mice stained for Oil red O (ORO) and hematoxylin. Oil red O positive muscle-adjacent adipocytes can be seen, frequently lipids smear into the muscle area close to these sites. However the majority of muscle tissue is free of ectopic lipid staining in control and in Nf1Myf5 mice (see inserts). (B) Images of hind limb cross sections of 1 week (top) and 12 week (bottom) control and Nf1Myf5 mice stained for Oil red O (ORO) and DAPI imaged with DIC optics. Top row in each panel shows muscle, bottom row shows

subcutaneous adipose tissue and adjacent muscle, where lipid droplet artefacts due to smearing can be observed.

Figure S6 Extended data for analysis of adipose tissue in Nf1Myf5 mice (A) RT-qPCR analysis of psWAT of 12 week old control vs. Nf1Myf5 mice for Cd36, Plin1, Pparg, mtCO1 and Cs (n=3 animals per genotype). (B) RT-qPCR analysis of interscapular brown adipose tissue (iBAT) of 12 week old control and Nf1Myf5 animals for mtCO1, Ucp1, Cs and Pparg mRNA (n=3 animals per genotype). Error bars represent standard error of means (SEM). P-value was calculated by two-sided unpaired t-test.

Data S1. Supporting Information (DESeq2 analysis of transcriptome data)

Data S2. Supporting Information (MaxQuant processed output files)

Data S3. Supporting Information (Differentially expressed proteins)

Table S1. Supporting Information (List of primers)

Conflict of interest

All authors declare that they have no conflict of interest.

References

- Ratner N, Miller SJ. A RASopathy gene commonly mutated in cancer: the neurofibromatosis type 1 tumour suppressor. *Nat Rev Cancer* 2015;**15**:290–301.
- Eleftheriou F, Kolanczyk M, Schindeler A, Viskochil DH, Hock JM, Schorry EK, et al. Skeletal abnormalities in neurofibromatosis type 1: approaches to therapeutic options. *Am J Med Genet A* 2009;**149A**:2327–2338.
- Johnson BA, MacWilliams B, Carey JC, Viskochil DH, D'Astous JL, Stevenson DA. Lower extremity strength and hopping and jumping ground reaction forces in children with neurofibromatosis type 1. *Hum Mov Sci* 2012;**31**:247–254.
- Johnson BA, MacWilliams BA, Carey JC, Viskochil DH, D'Astous JL, Stevenson DA. Motor proficiency in children with neurofibromatosis type 1. *Pediatr Phys Ther* 2010;**22**:344–348.
- Patel NB, Stacy GS. Musculoskeletal manifestations of neurofibromatosis type 1. *AJR Am J Roentgenol* 2012;**199**:W99–W106.
- Souza JF, Passos RL, Guedes AC, Rezende NA, Rodrigues LO. Muscular force is reduced in neurofibromatosis type 1. *J Musculoskelet Neuronal Interact* 2009;**9**:15–17.
- Cornett KM, North KN, Rose KJ, Burns J. Muscle weakness in children with neurofibromatosis type 1. *Dev Med Child Neurol* 2015;**57**:733–736.
- Summers MA, Quinlan KG, Payne JM, Little DG, North KN, Schindeler A. Skeletal muscle and motor deficits in Neurofibromatosis Type 1. *J Musculoskelet Neuronal Interact* 2015;**15**:161–170.
- Stevenson DA, Allen S, Tidyman WE, Carey JC, Viskochil DH, Stevens A, et al. Peripheral muscle weakness in RASopathies. *Muscle Nerve* 2012;**46**:394–399.
- Stevenson DA, Yang FC. The musculoskeletal phenotype of the RASopathies. *Am J Med Genet C Semin Med Genet* 2011;**157**:90–103.
- Bachman JF, Klose A, Liu W, Paris ND, Blanc RS, Schmalz M, et al. Prepubertal skeletal muscle growth requires Pax7-expressing satellite cell-derived myonuclear contribution. *Development* 2018;**145**.
- White RB, Bierinx AS, Gnocchi VF, Zammit PS. Dynamics of muscle fibre growth during postnatal mouse development. *BMC Dev Biol* 2010;**10**:21.
- Schiaffino S, Dyar KA, Ciciliot S, Blaauw B, Sandri M. Mechanisms regulating skeletal muscle growth and atrophy. *FEBS J* 2013;**280**:4294–4314.
- Egerman MA, Glass DJ. Signaling pathways controlling skeletal muscle mass. *Crit Rev Biochem Mol Biol* 2014;**49**:59–68.
- Schiaffino S, Reggiani C. Fiber types in mammalian skeletal muscles. *Physiol Rev* 2011;**91**:1447–1531.
- Talbot J, Maves L. Skeletal muscle fiber type: using insights from muscle developmental biology to dissect targets for susceptibility and resistance to muscle disease. *Wiley Interdiscip Rev Dev Biol* 2016;**5**:518–534.
- Kolanczyk M, Kossler N, Kuhnisch J, Lavitas L, Stricker S, Wilkening U, et al. Multiple roles for neurofibromin in skeletal development and growth. *Hum Mol Genet* 2007;**16**:874–886.
- Kuhnisch J, Seto J, Lange C, Schrof S, Stumpp S, Kobus K, et al. Multiscale, converging defects of macro-porosity, microstructure and matrix mineralization impact long bone fragility in NF1. *PLoS ONE* 2014;**9**:e86115.
- Kossler N, Stricker S, Rodelsperger C, Robinson PN, Kim J, Dietrich C, et al. Neurofibromin (NF1) is required for skeletal

- muscle development. *Hum Mol Genet* 2011;**20**:2697–2709.
20. Summers MA, Rupasinghe T, Vasiljevski ER, Evesson FJ, Mikulec K, Peacock L, et al. Dietary intervention rescues myopathy associated with neurofibromatosis type 1. *Hum Mol Genet* 2018;**27**:577–588.
 21. Logan M, Martin JF, Nagy A, Lobe C, Olson EN, Tabin CJ. Expression of Cre recombinase in the developing mouse limb bud driven by a *Prx1* enhancer. *Genesis* 2002;**33**:77–80.
 22. Sullivan K, El-Hoss J, Quinlan KG, Deo N, Garton F, Seto JT, et al. NF1 is a critical regulator of muscle development and metabolism. *Hum Mol Genet* 2014;**23**:1250–1259.
 23. Tallquist MD, Weismann KE, Hellstrom M, Soriano P. Early myotome specification regulates PDGFA expression and axial skeleton development. *Development* 2000;**127**:5059–5070.
 24. Vasyutina E, Lenhard DC, Wende H, Erdmann B, Epstein JA, Birchmeier C. RBP-J (Rbpsi) is essential to maintain muscle progenitor cells and to generate satellite cells. *Proc Natl Acad Sci U S A* 2007;**104**:4443–4448.
 25. Zhu Y, Romero MI, Ghosh P, Ye Z, Charnay P, Rushing EJ, et al. Ablation of NF1 function in neurons induces abnormal development of cerebral cortex and reactive gliosis in the brain. *Genes Dev* 2001;**15**:859–876.
 26. Muzumdar MD, Tasic B, Miyamichi K, Li L, Luo L. A global double-fluorescent Cre reporter mouse. *Genesis* 2007;**45**:593–605.
 27. Kulak NA, Pichler G, Paron I, Nagaraj N, Mann M. Minimal, encapsulated proteomic-sample processing applied to copy-number estimation in eukaryotic cells. *Nat Methods* 2014;**11**:319–324.
 28. Gielisch I, Meierhofer D. Metabolome and proteome profiling of complex I deficiency induced by rotenone. *J Proteome Res* 2015;**14**:224–235.
 29. Martens L, Hermjakob H, Jones P, Adamski M, Taylor C, States D, et al. PRIDE: the proteomics identifications database. *Proteomics* 2005;**5**:3537–3545.
 30. Subramanian A, Tamayo P, Mootha VK, Mukherjee S, Ebert BL, Gillette MA, et al. Gene set enrichment analysis: a knowledge-based approach for interpreting genome-wide expression profiles. *Proc Natl Acad Sci* 2005;**102**:15545–15550.
 31. Pesta D, Gnaiger E. High-resolution respirometry: OXPHOS protocols for human cells and permeabilized fibers from small biopsies of human muscle. *Methods Mol Biol* 2012;**810**:25–58.
 32. Liu Y, Beyer A, Aebersold R. On the dependency of cellular protein levels on mRNA abundance. *Cell* 2016;**165**:535–550.
 33. Chemello F, Bean C, Cancellara P, Laveder P, Reggiani C, Lanfranchi G. Microgenomic analysis in skeletal muscle: expression signatures of individual fast and slow myofibers. *PLoS ONE* 2011;**6**:e16807.
 34. Lynch CJ, Xu Y, Hajnal A, Salzberg AC, Kawasawa YI. RNA sequencing reveals a slow to fast muscle fiber type transition after olanzapine infusion in rats. *PLoS ONE* 2015;**10**:e0123966.
 35. Whalen RG, Johnstone D, Bryers PS, Butler-Browne GS, Ecob MS, Jaros E. A developmentally regulated disappearance of slow myosin in fast-twitch muscles of the mouse. *FEBS Lett* 1984;**177**:51–56.
 36. Ninfali C, Siles L, Darling DS, Postigo A. Regulation of muscle atrophy-related genes by the opposing transcriptional activities of ZEB1/CtBP and FOXO3. *Nucleic Acids Res* 2018;**46**:10697–10708.
 37. Lecker SH, Jagoe RT, Gilbert A, Gomes M, Baracos V, Bailey J, et al. Multiple types of skeletal muscle atrophy involve a common program of changes in gene expression. *FASEB J* 2004;**18**:39–51.
 38. Scheck JM, Hyatt JP, Raffaello A, Jagoe RT, Roy RR, Reggie Edgerton V, et al. Rapid disuse and denervation atrophy involve transcriptional changes similar to those of muscle wasting during systemic diseases. *FASEB J* 2007;**21**:140–155.
 39. Bodine SC, Latres E, Baumhueter S, Lai VK, Nunez L, Clarke BA, et al. Identification of ubiquitin ligases required for skeletal muscle atrophy. *Science* 2001;**294**:1704–1708.
 40. Ciaraldi TP, Cha BS, Park KS, Carter L, Mudaliar SR, Henry RR. Free fatty acid metabolism in human skeletal muscle is regulated by PPAR γ and RXR agonists. *Ann N Y Acad Sci* 2002;**967**:66–70.
 41. Cha BS, Ciaraldi TP, Carter L, Nikoulina SE, Mudaliar S, Mukherjee R, et al. Peroxisome proliferator-activated receptor (PPAR) γ and retinoid X receptor (RXR) agonists have complementary effects on glucose and lipid metabolism in human skeletal muscle. *Diabetologia* 2001;**44**:444–452.
 42. Amin RH, Mathews ST, Camp HS, Ding L, Leff T. Selective activation of PPAR γ in skeletal muscle induces endogenous production of adiponectin and protects mice from diet-induced insulin resistance. *Am J Physiol Endocrinol Metab* 2010;**298**:E28–E37.
 43. Sanchez-Gurmaches J, Guertin DA. Adipocyte lineages: tracing back the origins of fat. *Biochim Biophys Acta* 2014;**1842**:340–351.
 44. Brohmann H, Jagla K, Birchmeier C. The role of Lbx1 in migration of muscle precursor cells. *Development* 2000;**127**:437–445.
 45. Gensch N, Borchardt T, Schneider A, Riethmacher D, Braun T. Different autonomous myogenic cell populations revealed by ablation of Myf5-expressing cells during mouse embryogenesis. *Development* 2008;**135**:1597–1604.
 46. Comai G, Sambasivan R, Gopalakrishnan S, Tajbakhsh S. Variations in the efficiency of lineage marking and ablation confound distinctions between myogenic cell populations. *Dev Cell* 2014;**31**:654–667.
 47. Haldar M, Karan G, Tvrdik P, Capecchi MR. Two cell lineages, myf5 and myf5-independent, participate in mouse skeletal myogenesis. *Dev Cell* 2008;**14**:437–445.
 48. Haldar M, Karan G, Watanabe S, Guenther S, Braun T, Capecchi MR. Response: contributions of the Myf5-independent lineage to myogenesis. *Dev Cell* 2014;**31**:539–541.
 49. Joe AW, Yi L, Natarajan A, Le Grand F, So L, Wang J, et al. Muscle injury activates resident fibro/adipogenic progenitors that facilitate myogenesis. *Nat Cell Biol* 2010;**12**:153–163.
 50. Uezumi A, Fukada S, Yamamoto N, Takeda S, Tsuchida K. Mesenchymal progenitors distinct from satellite cells contribute to ectopic fat cell formation in skeletal muscle. *Nat Cell Biol* 2010;**12**:143–152.
 51. Uezumi A, Ito T, Morikawa D, Shimizu N, Yoneda T, Segawa M, et al. Fibrosis and adipogenesis originate from a common mesenchymal progenitor in skeletal muscle. *J Cell Sci* 2011;**124**:3654–3664.
 52. Vallecillo-García P, Orgeur M, Vom Hofe-Schneider S, Stumm J, Kappert V, Ibrahim DM, et al. Odd skipped-related 1 identifies a population of embryonic fibro-adipogenic progenitors regulating myogenesis during limb development. *Nat Commun* 2017;**8**:1–18.
 53. Stumm J, Vallecillo-García P, Vom Hofe-Schneider S, Ollitrault D, Schrewe H, Economides AN, et al. Odd skipped-related 1 (Osr1) identifies muscle-interstitial fibro-adipogenic progenitors (FAPs) activated by acute injury. *Stem Cell Res* 2018;**32**:8–16.
 54. Hasson P, DeLaurier A, Bennett M, Grigorieva E, Naiche LA, Papaioannou VE, et al. Tbx4 and tbx5 acting in connective tissue are required for limb muscle and tendon patterning. *Dev Cell* 2010;**18**:148–156.
 55. Chen JC, Mortimer J, Marley J, Goldhamer DJ. MyoD-cre transgenic mice: a model for conditional mutagenesis and lineage tracing of skeletal muscle. *Genesis* 2005;**41**:116–121.
 56. Summers MA, Vasiljevski ER, Mikulec K, Peacock L, Little DG, Schindeler A. Developmental dosing with a MEK inhibitor (PD0325901) rescues myopathic features of the muscle-specific but not limb-specific Nf1 knockout mouse. *Mol Genet Metab* 2018;**123**:518–525.
 57. van Wessel T, de Haan A, van der Laarse WJ, Jaspers RT. The muscle fiber type-fiber size paradox: hypertrophy or oxidative metabolism? *Eur J Appl Physiol* 2010;**110**:665–694.
 58. Niro C, Demignon J, Vincent S, Liu Y, Giordani J, Sgarioni N, et al. Six1 and Six4 gene expression is necessary to activate the fast-twitch muscle gene program in the mouse primary myotome. *Dev Biol* 2010;**338**:168–182.
 59. Hagiwara N, Yeh M, Liu A. Sox6 is required for normal fiber type differentiation of fetal skeletal muscle in mice. *Dev Dyn* 2007;**236**:2062–2076.
 60. Grifone R, Laclef C, Spitz F, Lopez S, Demignon J, Guidotti JE, et al. Six1 and Eya1 expression can reprogram adult muscle from the slow-twitch phenotype into the fast-twitch phenotype. *Mol Cell Biol* 2004;**24**:6253–6267.
 61. Lee KY, Singh MK, Ussar S, Wetzel P, Hirshman MF, Goodyear LJ, et al. Tbx15 controls skeletal muscle fibre-type determination and muscle metabolism. *Nat Commun* 2015;**6**:8054.

62. Baxendale S, Davison C, Muxworthy C, Wolff C, Ingham PW, Roy S. The B-cell maturation factor Blimp-1 specifies vertebrate slow-twitch muscle fiber identity in response to Hedgehog signaling. *Nat Genet* 2004;**36**:88–93.
63. Quiat D, Voelker KA, Pei J, Grishin NV, Grange RW, Bassel-Duby R, et al. Concerted regulation of myofiber-specific gene expression and muscle performance by the transcriptional repressor Sox6. *Proc Natl Acad Sci U S A* 2011;**108**:10196–10201.
64. Taglietti V, Maroli G, Cermenati S, Monteverde S, Ferrante A, Rossi G, et al. Nfix induces a switch in Sox6 transcriptional activity to regulate MyHC-I expression in fetal muscle. *Cell Rep* 2016;**17**:2354–2366.
65. Boyer JG, Prasad V, Song T, Lee D, Fu X, Grimes KM, et al. ERK1/2 signaling induces skeletal muscle slow fiber-type switching and reduces muscular dystrophy disease severity. *JCI Insight* 2019;**5**.
66. Arner P, Langin D. Lipolysis in lipid turnover, cancer cachexia, and obesity-induced insulin resistance. *Trends Endocrinol Metab* 2014;**25**:255–262.
67. Sanchez-Gurmaches J, Guertin DA. Adipocytes arise from multiple lineages that are heterogeneously and dynamically distributed. *Nat Commun* 2014;**5**:4099.
68. Sanchez-Gurmaches J, Hung CM, Sparks CA, Tang Y, Li H, Guertin DA. PTEN loss in the Myf5 lineage redistributes body fat and reveals subsets of white adipocytes that arise from Myf5 precursors. *Cell Metab* 2012;**16**:348–362.
69. Hotta Y, Nakamura H, Konishi M, Murata Y, Takagi H, Matsumura S, et al. Fibroblast growth factor 21 regulates lipolysis in white adipose tissue but is not required for ketogenesis and triglyceride clearance in liver. *Endocrinology* 2009;**150**:4625–4633.
70. Han J, Meng Q, Shen L, Wu G. Interleukin-6 induces fat loss in cancer cachexia by promoting white adipose tissue lipolysis and browning. *Lipids Health Dis* 2018;**17**:14.
71. Kelly M, Gauthier MS, Saha AK, Ruderman NB. Activation of AMP-activated protein kinase by interleukin-6 in rat skeletal muscle: association with changes in cAMP, energy state, and endogenous fuel mobilization. *Diabetes* 2009;**58**:1953–1960.
72. Febbraio MA, Hiscock N, Sacchetti M, Fischer CP, Pedersen BK. Interleukin-6 is a novel factor mediating glucose homeostasis during skeletal muscle contraction. *Diabetes* 2004;**53**:1643–1648.
73. Carey AL, Steinberg GR, Macaulay SL, Thomas WG, Holmes AG, Ramm G, et al. Interleukin-6 increases insulin-stimulated glucose disposal in humans and glucose uptake and fatty acid oxidation in vitro via AMP-activated protein kinase. *Diabetes* 2006;**55**:2688–2697.
74. Krause MP, Liu Y, Vu V, Chan L, Xu A, Riddell MC, et al. Adiponectin is expressed by skeletal muscle fibers and influences muscle phenotype and function. *Am J Physiol Cell Physiol* 2008;**295**:C203–C212.
75. Hevener AL, He W, Barak Y, Le J, Bandyopadhyay G, Olson P, et al. Muscle-specific Pparg deletion causes insulin resistance. *Nat Med* 2003;**9**:1491–1497.
76. Norris AW, Chen L, Fisher SJ, Szanto I, Ristow M, Jozsi AC, et al. Muscle-specific PPAR γ -deficient mice develop increased adiposity and insulin resistance but respond to thiazolidinediones. *J Clin Invest* 2003;**112**:608–618.
77. Keipert S, Ost M, Johann K, Imber F, Jastroch M, Van Schothorst EM, et al. Skeletal muscle mitochondrial uncoupling drives endocrine cross-talk through the induction of FGF21 as a myokine. *Am J Physiol Endocrinol Metab* 2014;**306**:E469–E482.
78. Tezze C, Romanello V, Desbats MA, Fadini GP, Albiero M, Favaro G, et al. Age-associated loss of OPA1 in muscle impacts muscle mass, metabolic homeostasis, systemic inflammation, and epithelial senescence. *Cell Metab* 2017;**25**:1374, e1376–1389.
79. Forsstrom S, Jackson CB, Carroll CJ, Kuronen M, Pirinen E, Pradhan S, et al. Fibroblast growth factor 21 drives dynamics of local and systemic stress responses in mitochondrial myopathy with mtDNA deletions. *Cell Metab* 2019;**30**:1040, e1047–1054.
80. Oost LJ, Kustermann M, Armani A, Blaauw B, Romanello V. Fibroblast growth factor 21 controls mitophagy and muscle mass. *J Cachexia Sarcopenia Muscle* 2019;**10**:630–642.
81. Liang X, Liu L, Fu T, Zhou Q, Zhou D, Xiao L, et al. Exercise inducible lactate dehydrogenase B regulates mitochondrial function in skeletal muscle. *J Biol Chem* 2016;**291**:25306–25318.
82. Souza MLR, Jansen AK, Rodrigues LOC, Vilela DLS, Kakehasi AM, Martins AS, et al. Increased resting metabolism in neurofibromatosis type 1. *Clin Nutr ESPEN* 2019;**32**:44–49.
83. Dard L, Bellance N, Lacombe D, Rossignol R. RAS signalling in energy metabolism and rare human diseases. *Biochim Biophys Acta Bioenerg* 2018;**1859**:845–867.
84. Kimmelman AC. Metabolic dependencies in RAS-driven cancers. *Clin Cancer Res* 2015;**21**:1828–1834.
85. Lin SC, Hardie DG. AMPK: sensing glucose as well as cellular energy status. *Cell Metab* 2018;**27**:299–313.
86. Kjobsted R, Hingst JR, Fentz J, Foretz M, Sanz MN, Pehmoller C, et al. AMPK in skeletal muscle function and metabolism. *FASEB J* 2018;**32**:1741–1777.
87. Murphy MP. How mitochondria produce reactive oxygen species. *Biochem J* 2009;**417**:1–13.
88. Abrigo J, Elorza AA, Riedel CA, Vilos C, Simon F, Cabrera D, et al. Role of oxidative stress as key regulator of muscle wasting during cachexia. *Oxid Med Cell Longev* 2018;**2018**:2063179.
89. Sullivan-Gunn MJ, Campbell-O'Sullivan SP, Tisdale MJ, Lewandowski PA. Decreased NADPH oxidase expression and antioxidant activity in cachectic skeletal muscle. *J Cachexia Sarcopenia Muscle* 2011;**2**:181–188.
90. Tong JJ, Schriener SE, McCleary D, Day BJ, Wallace DC. Life extension through neurofibromin mitochondrial regulation and antioxidant therapy for neurofibromatosis-1 in *Drosophila melanogaster*. *Nat Genet* 2007;**39**:476–485.
91. Ferreira LF, Laitano O. Regulation of NADPH oxidases in skeletal muscle. *Free Radic Biol Med* 2016;**98**:18–28.
92. von Haehling S, Morley JE, Coats AJS, Anker SD. Ethical guidelines for publishing in the *Journal of Cachexia, Sarcopenia and Muscle*: update 2019. *J Cachexia Sarcopenia Muscle* 2019;**10**:1143–1145.